

IMPACT OF CENTRALITY DEFINITIONS AND DEUTERON
FORMATION ON FLUCTUATION OBSERVABLES IN HEAVY ION
COLLISIONS



A Thesis Submitted in Partial Fulfillment of the Requirements for the
Degree of Doctor of Philosophy in Physics
Suranaree University of Technology
Academic Year 2022

ผลกระทบของการนิยามเซนทร์ลลิตีและรูปแบบการเกิดดิวิเทอร์รอนต่อความ
แปรปรวนของปริมาณที่ตรวจวัดได้ในการชนกันของไอออนหนัก



นางสาวสุกัญญา สมบุญ

วิทยานิพนธ์นี้เป็นส่วนหนึ่งของการศึกษาตามหลักสูตรปริญญาวิทยาศาสตรดุษฎีบัณฑิต
สาขาวิชาฟิสิกส์
มหาวิทยาลัยเทคโนโลยีสุรนารี
ปีการศึกษา 2565

IMPACT OF CENTRALITY DEFINITIONS AND DEUTERON FORMATION ON
FLUCTUATION OBSERVABLES IN HEAVY ION COLLISIONS

Suranaree University of Technology has approved this thesis submitted in partial fulfillment of the requirements for the Degree of Doctor of Philosophy.

Thesis Examining Committee



(Assoc. Prof. Dr. Panomsak Meemon)

Chairperson



(Assoc. Prof. Dr. Ayut Limphirat)

Member (Thesis Advisor)



(Prof. Dr. Yupeng Yan)

Member



(Prof. Dr. Marcus Bleicher)

Member



(Assoc. Prof. Dr. Pornrad Srisawad)

Member



(Asst. Prof. Dr. Christoph Herold)

Member



(Assoc. Prof. Dr. Yupaporn Ruksakulpiwat)

Vice Rector for Academic Affairs
and Quality Assurance



(Prof. Dr. Santi Maensiri)

Dean of Institute of Science

สุกัญญา สมบุญ : ผลกระทบของการนิยามเซนทรัลลิตีและรูปแบบการเกิดดิวเทอรอน ต่อความแปรปรวนของปริมาณที่ตรวจวัดได้ในการชนกันของไอออนหนัก (IMPACT OF CENTRALITY DEFINITIONS AND DEUTERON FORMATION ON FLUCTUATION OBSERVABLES IN HEAVY ION COLLISIONS) อาจารย์ที่ปรึกษา : รองศาสตราจารย์ ดร.อายุทส ลัมพิตร์, 74 หน้า

คำสำคัญ: แบบจำลอง UrQMD, จำนวนโปรตอนสุทธิ, เคอร์โทซิส, การนิยามเซนทรัลลิตี, การเกิดดิวเทอรอน

วิทยานิพนธ์นี้ได้ใช้แบบจำลอง UrQMD เพื่อศึกษาผลกระทบของการนิยามเซนทรัลลิตี ช่วงของโมเมนตัมตามขวาง ความกว้างของแรพิดิตีและประสิทธิภาพของเครื่องตรวจจับต่อค่าเคอร์โทซิสของจำนวนโปรตอนสุทธิในการชนกันของ Au+Au ที่ระดับพลังงาน $\sqrt{s_{NN}} = 7.7$ GeV พบว่าการนิยามเซนทรัลลิตีที่แตกต่างกันนำไปสู่ค่าเคอร์โทซิสที่แตกต่างกัน รวมถึงช่วงของโมเมนตัมตามขวาง และความกว้างของแรพิดิตียังมีผลต่อค่าเคอร์โทซิสอีกด้วย ค่าเคอร์โทซิสของจำนวนโปรตอนสุทธิมีค่าเพิ่มขึ้นเมื่อเพิ่มประสิทธิภาพของเครื่องตรวจจับสำหรับจำนวนอนุภาคที่มีประจุสุทธิ นอกจากนี้แบบจำลอง UrQMD+coalescence ถูกนำมาใช้เพื่อคำนวณการเกิดดิวเทอรอน ซึ่งผลการคำนวณในวิทยานิพนธ์นี้ถูกนำมาเปรียบเทียบกับข้อมูลผลการทดลอง พบว่ากระบวนการเกิดดิวเทอรอนซึ่งพิจารณาจากผลการกระจายแรพิดิตีและโมเมนตัมตามขวางในการชนแบบ p + p, p + A และ A + A นั้นสอดคล้องกับข้อมูลการทดลองเป็นอย่างดี แสดงให้เห็นว่าแบบจำลอง UrQMD+coalescence ด้วยพารามิเตอร์ $\Delta p_{max} = 0.285$ GeV และ $\Delta r_{max} = 3.575$ fm สามารถใช้อธิบายการเกิดดิวเทอรอนได้เป็นอย่างดี

สาขาวิชาฟิสิกส์
ปีการศึกษา 2565

ลายมือชื่อนักศึกษา กัญญา สมบุญ
ลายมือชื่ออาจารย์ปรึกษา อายุทส ลัมพิตร์

SUKANYA SOMBUN : IMPACT OF CENTRALITY DEFINITIONS AND DEUTERON FORMATION ON FLUCTUATION OBSERVABLES IN HEAVY ION COLLISIONS.
THESIS ADVISOR : ASST. PROF. AYUT LIMPHIRAT, Ph.D. 74 PP.

Keyword: UrQMD model, Net-proton number, Kurtosis, Centrality definitions, Deuteron productions

In this thesis, the UrQMD model is used to investigate the impact of the centrality definition, transverse momentum (p_T) acceptance, rapidity window and detector efficiency on kurtosis of the net-proton number in Au+Au collisions at $\sqrt{s_{NN}} = 7.7$ GeV with minimum bias. It is found that different centrality definitions lead to different values of kurtosis. The dependence of p_T acceptance and rapidity window on kurtosis are also shown in this work. The kurtosis of the net-proton increases with increasing detector efficiency for N_{charge} . Moreover, the UrQMD model with coalescence is used to calculate the production of deuterons. Our results are compared with available experimental data. It is found that the production process of deuterons, as reflected in their rapidity and transverse momentum distributions in $p + p$, $p + A$, and $A + A$ collisions, are in good agreement with experimental data. It is demonstrated that the UrQMD+coalescence model with parameters $\Delta p_{max} = 0.285$ GeV/c and $\Delta r_{max} = 3.575$ fm provides a very good description of the available data on deuteron production.

School of Physics
Academic Year 2022

Student's Signature Subanya Sombun
Advisor's Signature

ACKNOWLEDGEMENTS

I am most appreciative to my advisor, Assoc. Prof. Dr. Ayut Limphirat, for his assistance, time, and counsel. Without his advice, enthusiasm, extensive knowledge of physics, and spiritual outlook, this thesis would not have been possible.

I would like to acknowledge Prof. Dr. Marcus Bleicher and Dr. Jan Steinhilber for their invaluable guidance on the research subject during my thesis at the Institute for Theoretical Physics, Frankfurt University, Germany.

I would like to thank Dr. Kristiya Tomuang and Dr. Paula Hillmann for their cooperation on this work.

I would like to express thanks for the support of Thailand Research Fund (TRF-RGJ PHD/0185/2558), Deutscher Akademischer Austauschdienst (DAAD), HIC for FAIR and Center of Excellence in High Energy Physics and Astrophysics (COE). Thanks are also extended to our theoretical physics group at Suranaree University of Technology, as well as the group's instructors and members, for their insightful teachings, discussions, and instruction.

I would like to acknowledge the computational resources provided by the LOEWE Frankfurt Center for Scientific Computing (LOEWE-CSC) and the Center for Computer Services at SUT.

Finally, I am thankful to my parents and companions for their endless support, encouragement and inspiration throughout my years of study.

Sukanya Sombun

CONTENTS (Continued)

	Page
2.1.5 Reaction channel	25
Resonances	25
Strings	26
2.2 Cumulants	29
2.3 Statistical Error	32
III HIGHER ORDER CUMULANTS OF NET-PROTON NUMBER ON THE CENTRALITY DEFINITION	33
3.1 Centrality Definition	33
3.2 Dependence on centrality definition	37
3.3 Effects of transverse momentum (p_T) acceptance	39
3.4 Effects of efficiency	40
3.5 Effects of rapidity dependence	42
IV DEUTERON PRODUCTION	44
4.1 Proton-induced reaction	46
4.2 Nucleus-nucleus reaction	48
4.3 Excitation function	53
V CONCLUSIONS	59
REFERENCES	61
APPENDICES	
APPENDIX A LORENTZ TRANSFORMATION	71
APPENDIX B KINEMATIC VARIABLES	72
CURRICULUM VITAE	74

LIST OF TABLES

Table		Page
2.1	With and without the Pauli potential, the parameters for implementing the rigid equation of state in the UrQMD model are listed below.	17
2.2	ID of baryon and baryon-resonances used in UrQMD model.	18
2.3	Mesons and meson resonance are arranged in the UrQMD model in accordance with spin and parity.	19
2.4	The CERN/HERA parameterization parameters for the elastic and total cross sections of $\bar{p}p$. This parameters is used in UrQMD for $p_{\text{lab}} > 5 \text{ GeV}/c$	21
2.5	The cross section of baryon-baryon reactions in [mb] according to the Additive Quark Model. The baryon-baryon scattering is demonstrated explicitly.	24
2.6	The cross-section of meson-bayron reactions in [mb] according to the Additive Quark Model. The meson-bayron scattering in the resonance region ($\sqrt{s} < 1.7 \text{ GeV}$) is demonstrated explicitly.	25
2.7	The cross-sections of meson-meson reactions in [mb] according to the Additive Quark Model. The meson-meson scattering in the resonance region ($\sqrt{s} < 1.7 \text{ GeV}$) is demonstrated explicitly.	25
2.8	Masses (GeV/c^2), widths (MeV) and branching ratios of non-strange baryon-resonances in UrQMD model. All parameters are given by the Review of Particle Properties (Barnett et al., 1996).	27
2.9	Probabilities for the different meson multiplets.	29
4.1	The integrated yield (dN/dy) of deuterons and anti-deuterons in p+p collisions with midrapidity $ y < 0.5$ at different center of mass energies as $\sqrt{s_{\text{NN}}} = 0.9, 2.76$ and 7 TeV.	47

LIST OF FIGURES

Figure		Page
1.1	The QCD phase diagram of nuclear matter at temperature (T) and chemical baryon potential (μ_B). The solid white line is the first-order phase transition and the end point (solid circle) of this transition is the QCD critical point (Nayak, 2020).	3
1.2	The results of R_{AA} of Au+Au collision at $\sqrt{s_{NN}} = 200$ GeV as a function of p_T at RHIC.	4
1.3	Left: the QCD phase diagram from the σ field model. Right: A non-monotonic energy dependence of the distribution of fourth order cumulants ($\kappa_4 = \langle (\delta N)^4 \rangle_c / \langle N \rangle$) (Luo and Xu, 2017).	9
1.4	Energy dependence of cumulant ratios of the net-proton distributions for 0 – 5% central Au+Au collisions at $\sqrt{s_{NN}} = 7.7$ to 200 GeV and compared with the HRG and UrQMD models.	10
2.1	The UrQMD parameterization of $\bar{p}p$ cross sections compared with experiment data (Barnett et al., 1996) The diffractive cross section is the difference between the total cross section and the sum of elastic and annihilation cross sections. . .	20
2.2	The total cross-section of K^-p interaction as a function of laboratory momentum (p_{lab}). The data are taken from (Zyla et al., 2020).	23
2.3	The total cross-section of K^+p interaction as a function of laboratory momentum (p_{lab}). The data are taken from (Zyla et al., 2020).	24
2.4	Particle production resulting from string excitation.	28

LIST OF FIGURES (Continued)

Figure		Page
2.5	Difference of the skewness distribution (Sheskin, 2003). . .	31
2.6	Difference of the kurtosis distribution. (Glen, 2017).	31
3.1	Left: Two nuclei before collision with impact parameter b . Right: participant and spectator nucleons during collision. .	34
3.2	Distributions of N_{charge} , N_{part} and $N_{\text{part-projectile}}$ in minimum bias Au+Au collisions at $\sqrt{s_{\text{NN}}}=7.7$ GeV.	35
3.3	Distribution of N_{charge} as a function of N_{part} for 11 million minimum bias events.	36
3.4	The correlation coefficient between N_{charge} and N_{part} or $N_{\text{part-projectile}}$ as a function of impact parameter in Au+Au collisions at $\sqrt{s_{\text{NN}}}=7.7$ GeV. The circle line denotes correlation between N_{part} and N_{charge} . The square line denotes correlation between $N_{\text{part-projectile}}$ and N_{charge}	37
3.5	The ratios of cumulant of the net-proton number distributions as a function of centrality which is defined by N_{part} . It is shown in Figure 3.5. The square line denotes first method, the circle line denotes second method, the square line denotes third method and the grey band indicates the statistical error.	38
3.6	The results of $\kappa\sigma^2$ of the net-proton number as a function of centrality for the three centrality definitions at mid-rapidity $ y < 0.5$ and within transverse momentum $0.4 < p_{\text{T}} < 0.8$ GeV. The square line denotes centrality as defined by N_{charge} , while the circle and triangle lines denote centrality as defined by N_{part} and $N_{\text{part-projectile}}$, respectively. . .	40
3.7	The kurtosis of the net-proton number as a function of centrality which is defined by N_{charge} for two different p_{T} acceptance. The square line denotes $0.4 < p_{\text{T}} < 0.8$ GeV and the circle line denotes $0.4 < p_{\text{T}} < 2.0$ GeV.	41

LIST OF FIGURES (Continued)

Figure		Page
3.8	The kurtosis of the net-proton number as a function of centrality (defined by N_{charge}) within two different p_T acceptance.	42
3.9	The result of cumulant ratios of net-proton number as a function of centrality which is defined by 70% N_{charge} efficiency within $0.4 < p_T < 2.0$ GeV. The circle line denotes the proton efficiency at 100% (true), the square line denotes the proton efficiency at 75% (uncorrected).	43
3.10	The dependence of the kurtosis and skewness of proton number on the size of the rapidity window, $0.0 \leq y \leq 2.0$, within $0.4 < p_T < 2.0$ GeV.	43
4.1	Rapidity distributions of protons and deuterons in minimum bias p+Be (left) and p+Au (right) collisions at a beam energy of 14.6A GeV. The lines indicate the UrQMD calculations and the solid circle denotes the E802 experimental data (Abbott et al., 1993).	47
4.2	Energy dependence of d/p and \bar{d}/\bar{p} ratios in pp collisions with $ y < 0.5$ at $\sqrt{s_{\text{NN}}} = 53, 900, 2760$ and 7000 GeV. The open circle and triangle are calculated by the UrQMD model, the solid star denotes the results from ISR (Alper et al., 1973; Henning et al., 1978; Alper et al., 1975) and the solid circle and triangle denote the results from ALICE experimental data.	48
4.3	The $dN/dy^{(0)}$ distributions of deuterons, protons and π^- for Ni+Ni collisions with $b \leq 1.8$ at beam energies of 1.93A, 1.45A and 1.06A GeV. The lines indicate the UrQMD model and the circle symbols denote the FOPI experiment (Hong et al., 1998).	49

LIST OF FIGURES (Continued)

Figure		Page
4.4	Rapidity distributions of protons and deuterons (times 5) in Au+Au collisions at a beam energy of 10.8A GeV with $b = 3$ fm. The dashed line indicates our simulation and the circle symbol denotes the E917 experimental data (Back et al., 2001).	51
4.5	Invariant yields of deuterons at $p_t = 0$ as a function of rapidity in central (left) and minimum-bias (right) Au+Au collisions at a beam energy of 10.8A GeV. The lines denote the UrQMD model calculations, the circle symbol denotes the E878 experiment data (Bennett et al., 1998).	52
4.6	Rapidity distributions of protons and deuterons in Si+Au collisions at a beam energy of 14.6A GeV with impact parameter $b = 2$ fm. The lines indicate our model calculations and the circle symbols denote the E802 experimental data (Abbott et al., 1994).	53
4.7	Invariant yields of deuterons at $p_t = 0$ as a function of rapidity in central (left) and minimum-bias (right) Si+Pb collisions at a beam energy of 14.6A GeV. The lines indicate the UrQMD calculations and the circle symbols denote the E814 experimental data (Anticic et al., 2016)	54
4.8	Invariant yields of deuterons as a function of $m_t - m$ in central Si+Al, Si+Cu and Si+Au collisions at a beam energy of 14.6A GeV. The rapidity interval is $y = 0.5$ to 1.5 with $\Delta y = 0.2$. Each successive spectrum is divided by 100 for visual clarity. The circle symbols denote the E802 experimental data (Abbott et al., 1994) and the lines indicate the UrQMD calculations.	55

LIST OF FIGURES (Continued)

Figure		Page
4.9	Deuteron distributions as a function of rapidity in Pb+Pb collisions at a beam energy of 20A GeV for different centralities. The lines denote the UrQMD calculations and the circle symbols denote the NA49 experimental data (Anticic et al., 2016) and the lines denote the UrQMD calculations.	55
4.10	Deuteron distributions as a function of rapidity at beam energies 20A GeV, 30A GeV, 40A GeV, 80A GeV, and 158A GeV in central Pb+Pb collisions. The circle symbols denote the NA49 experimental data (Anticic et al., 2016) and the lines show the UrQMD calculations. Each spectrum are successively divided by a factor of 10.	56
4.11	The invariant yields of anti-deuterons (\bar{d}) and anti-protons (\bar{p}) at $p_t = 0$ as a function of rapidity in Si+Au collisions at a beam energy of 14.6A GeV with $b = 2$ fm. Our results are compared to the data from the E858 (Shiva et al., 1994) and E814 (Barrette et al., 1993) experiments. The lines denote the UrQMD calculation The circle symbols denote the E858 and E814 experimental data.	57
4.12	The ratio of deuteron to proton ratio and a function of energy dependence in Au+Au collisions with $b \leq 4.6$ fm and $ y < 0.3$. The solid lines denote UrQMD model results, the dotted lines denote the thermal model fit (Andronic et al., 2011) and symbols denote experimental data from various collaborations (triangle down: SIS (Cleymans et al., 1999), hexagon: E802 (Ahle et al., 1999), triangles up: PHENIX (Adler et al., 2005), diamonds: NA49 (Anticic et al., 2016), circles: STAR (Yu, 2017), pentagon: ALICE (Anielski, 2015), square: E814 (Barrette et al., 1993).	58

CHAPTER I

INTRODUCTION

Our early universe was most likely an extremely hot and dense form of matter. At time 10^{-12} s after the big bang, hadronic soup consist of quarks and gluons. The property of Quantum Chromodynamics (QCD) (Gross and Wilczek, 1973) predicts that such a phase of deconfined quarks and gluons, known as the Quark- Gluon Plasma (QGP) existed (Shuryak, 1978). At 10^{-6} s after Big-Bang, the universe has reached a temperature. Where the QCD phase transition took place and quarks became confined into hadrons.

Because our world is limited to confined matter, we cannot directly measure the properties of quarks and gluons. Thus, we are focused on signals in the later stages of a cooled fireball produced in Heavy-ion collisions (HIC) following its hadronization. Some of the common signals for QGP are jet quenching, dilepton production, strangeness enhancement, charmonium suppression, and anisotropic.

Exploring the QCD phase structure is one of the primary objectives of research involving heavy ion collisions at high beam energies which is the possible existence of a first order phase transition which ends in a critical endpoint, located at high temperature and non-zero baryon chemical potential. It is one of the main goals of the Beam Energy Scan (BES) program at the Relativistic Heavy-Ion Collider (RHIC) (Aggarwal et al., 2010), which is located at the Brookhaven National Laboratory (BNL) in the United States and the Large Hadron Collider (LHC) at the European Organization for Nuclear Research (CERN). It also motivates for the research programs at the future accelerator facilities FAIR in Darmstadt and NICA in Dubna.

1.1 QCD Phase Diagram

Thermodynamic properties of a system are expressed in the terms of a phase diagram. Changes in the relevant thermodynamic variables lead to phase transition in the system. Phase transitions are divided into first-order, second-order, and crossover transitions. The first-order phase transition is characterized

by a discontinuity in one of the first derivatives of the thermodynamic potential, e.g., the density, and it allows for coexistence of two phases at a certain transition point. At arrive at a point where the two phases can no longer be distinguished. Here, the density changes continuously and a discontinuity can only be found in a second derivative of the thermodynamic potential. One speaks of a second-order phase transition or critical point. If the characteristic observable changes rapidly but smoothly, the transition is called a crossover.

The QCD phase diagram is often depicted as a function of temperature (T) and baryon chemical potential (μ) which is associated with the net-baryon number. As show in Figure 1.1, tattie QCD calculation predict a crossover transition at zero baryon chemical potential ($\mu_B = 0$) and around a critical temperature $T_c \sim 150 - 160$ MeV (Cheng et al., 2006) between hadronic and quark-gluon phase. At large baryon chemical potential, QCD based models predict the possible existence of the endpoint of the first order phase transition in the QCD phase diagram. The experimentalists attempt to vary the temperature and baryon chemical potential of the nuclear matter created in heavy-ion collisions. It is expected that fluctuations of conserved quantities yield information on the QCD phase structure it the freeze-out is sufficiently close to the phase boundary.

1.2 Signals of The Quark Gluon Plasma

Undoubtedly, identifying the QGP phase is one of the most difficult aspects of heavy-ion collision experiments. However, since the evolution of the earliest phases of the universe cannot be directly measured, we do not have a direct understanding of their development. The HIC signatures are analyzed. Among the primary characteristics of QGP are jet suppression, oddity enhancement, collective flow and fluctuation etc. The most integral ones to this thesis are fluctuation.

1.2.1 Jet Quenching

In QCD, when a parton in a nucleus scatters off of a parton in another nucleus is called jets. After the scattering, the parton are formed a parton shower leading to a spray of hadrons. The propagation of partons through a hot and dense medium modifies their transverse momentum (p_T) due to induced

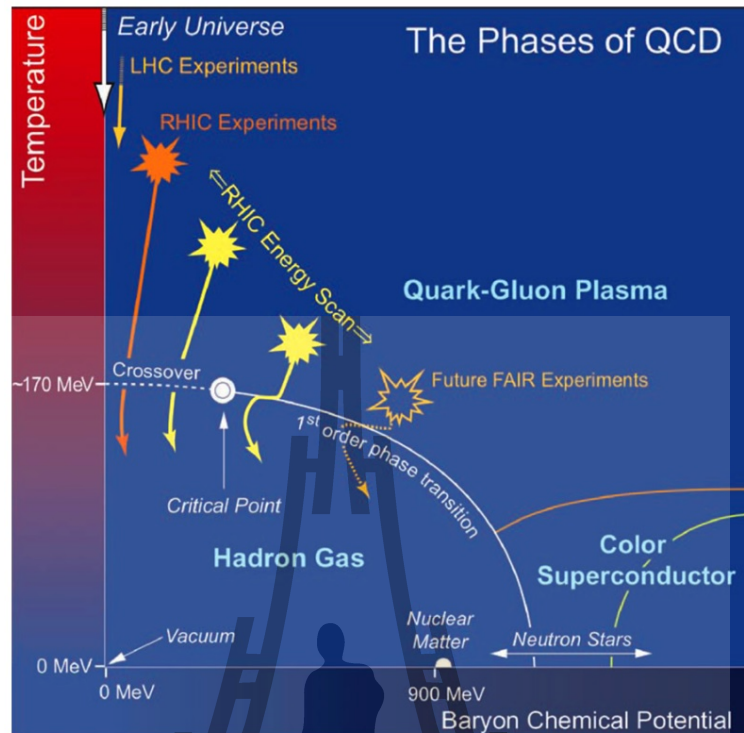


Figure 1.1 The QCD phase diagram of nuclear matter at temperature (T) and chemical baryon potential (μ_B). The solid white line is the first-order phase transition and the end point (solid circle) of this transition is the QCD critical point (Nayak, 2020).

energy loss, this energy loss of parton is known as jet quenching. Jet quenching is investigated by measurement of jets which can be used to determine the properties of the QGP.

Jet quenching can be measured by using the nuclear modification factor (R), which is defined as

$$R_{AA} = \frac{1}{N_{\text{coll}}} \frac{d^2 N_{AA} / dy d^2 p_T}{d^2 N_{pp} / dy d^2 p_T}, \quad (1.1)$$

where N_{coll} is the number of binary collisions in nucleus-nucleus (AA) collisions. If collisions between nucleus are a superposition of collisions between protons, then: $R_{AA} = 1$, indicating the absence of any medium. An $R_{AA} < 1$ indicates suppression and an $R_{AA} > 1$ indicates enhancement. The RHIC experiment shows the result of R_{AA} of Au+Au collision at $\sqrt{s_{NN}} = 200$ GeV as a function of p_T , as shown in Figure 1.2 (Kormilitzin et al., 2011). It is found that the

results of R_{AA} of hadron production for $p_T > 4\text{GeV}/c$ is less than unity. It means that the interaction of the high energy jets with the thermal medium is formed by the nuclear collisions.

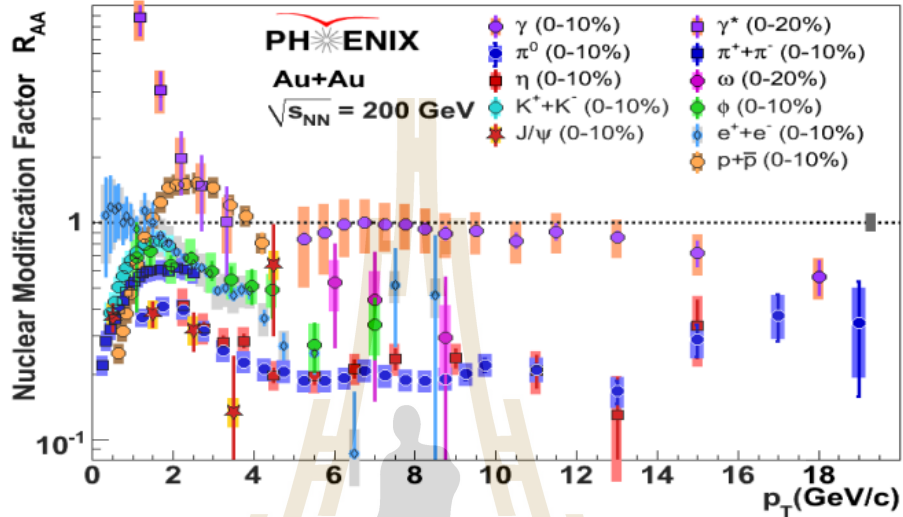


Figure 1.2 The results of R_{AA} of Au+Au collision at $\sqrt{s_{NN}} = 200$ GeV as a function of p_T at RHIC.

1.2.2 Strangeness Enhancement

In heavy ion collisions, a strangeness enhancement is observed to research excited nuclear matter and investigate the transition from hadronic matter to quark-gluon matter. Strange particle production is enhanced in the QGP with respect to a hadron gas. In comparison to the hadronic scenario, the time required for the thermalization of strangeness is drastically reduced as a result of the enhancement of strangeness production in different channels. This is supported by the difference in threshold energies due to the fact that odd quarks must be produced only in a deconfined state. In a QGP, strange quarks are created through gluon fusion $q\bar{q} \rightarrow s\bar{s}$ and light $q\bar{q}$ pair annihilation $q\bar{q} \rightarrow s\bar{s}$ processes. The threshold energy necessary to produce a pair of $s\bar{s}$ quarks in the QGP is simply the mass of the two unusual quarks ($E_{\text{threshold}} \approx 300\text{MeV}$). The process of light quarks by using Pauli blocking is an additional source of enhanced $s\bar{s}$ production. Therefore, the collision produces more light quarks. To create $s\bar{s}$ the available energy level must be filled.

The additional mechanisms for $s\bar{s}$ production in a QGP are predicted to result in a production rate that is 10 to 30 times greater than in a hadron gas, resulting in an equilibration of strangeness even during the brief duration of the the fireball. Consequently, it is supposed that the production of strange and anti-strange particles at freeze-out will be greater if the system proceeds through a deconfined phase as opposed to one that remained in the hadronic phase. Moreover, strangeness enhancement of the (anti-)hyperon yields (Λ , Ω , Ξ) in Pb-Pb collisions as compared to p-Pb collisions has been measured by the WA97 and NA57 Collaborations (Caliandro et al., 1999; Evans et al., 1999; Gabler et al., 1999; Margetis et al., 1999). It was found that the measured enhancement increases with the strangeness content of the particle.

1.2.3 Collective Flow

The collective flow in heavy ion collisions is one of the experimental and theoretical instruments used to study the properties of heated and dense nuclear matter. The transverse flow is connected to the pressure gradients in the initial overlap region of the colliding nuclei. Therefore, the flow is sensitive to the equation of state (EoS) and may be used to investigate phase transitions in QGP. Over the past two decades, the collective flow has been investigated to provide an overview of the corresponding theoretical investigations (Poskanzer and Voloshin, 1998; Bleicher and Stoecker, 2002; Yin et al., 2017; Retinskaya et al., 2012) and the experiment (Alt et al., 2003; Liu et al., 2000; Adamczyk et al., 2014; Andronic et al., 2005). The collective flow is given as the fourier expansion of the momentum distribution (Poskanzer and Voloshin, 1998)

$$E \frac{d^3N}{d^3p} = \frac{1}{2\pi} \frac{d^2N}{p_T d_{p_T} dy} \left(1 + 2 \sum_{n=1}^{\infty} v_n \cos[n(\varphi - \psi_{RP})] \right) \quad (1.2)$$

where ψ_{RP} denotes the reaction plane angle and φ is the azimuthal angle. Due to the symmetry of reflection with respect to the reaction plane, the sine terms in such an expansion disappear. The coefficients of Fourier, also known as v_n , are expressed by

$$v_n(p_T, y) = \langle \cos[n(\varphi - \psi_{RP})] \rangle \quad (1.3)$$

where $\langle \rangle$ denotes an average over all particles in all events.

1.3 Fluctuations

Event-by-event fluctuations of conserved quantities, such as electric charge, baryon number and strangeness, are used to explore phase transitions in the QCD phase structure. We investigate a system in grand canonical ensemble (thermal equilibrium) where the pressure of a thermal system is related to the logarithm of the partition function, which is characterized by

$$P = \frac{T}{V} \ln Z(T, V, \mu), \quad (1.4)$$

where V is the volume, T is the temperature and μ is the chemical potential. The particle number is obtained as

$$\langle N \rangle = \frac{1}{Z} \sum N e^{-\frac{(\epsilon - \mu N)}{T}}. \quad (1.5)$$

The susceptibility of conserved quantities is defined as the pressure derivative relative to the chemical potential. The generalized susceptibilities as

$$\chi_n = \frac{\partial^n (P/T^4)}{\partial (\mu/T)^n}. \quad (1.6)$$

The cumulants are related to the susceptibility of the system by

$$C_n = \frac{\partial^n \ln Z(V, T, \mu)}{\partial (\mu/T)^n} \quad (1.7)$$

$$= VT^3 \chi_n(T, \mu), \quad (1.8)$$

where n is the n^{th} order cumulants. Thus, it is straightforward to show that

$$C_1 = VT^3 \chi_1 = \langle N \rangle = M, \quad (1.9)$$

$$C_2 = VT^3 \chi_2 = \langle (\delta N)^2 \rangle = \sigma^2, \quad (1.10)$$

$$C_3 = VT^3 \chi_3 = \langle (\delta N)^3 \rangle = S\sigma^3, \quad (1.11)$$

$$C_4 = VT^3 \chi_4 = \langle (\delta N)^4 \rangle - 3\langle (\delta N)^2 \rangle^2 = \kappa\sigma^4, \quad (1.12)$$

where M , σ^2 , S , κ are Mean, Variance, Skewness and Kurtosis and $(\delta N) = N - \langle N \rangle$. These variables will be discussed in Chapter 11. In experiment, the dependence on volume and temperature is hard to study. Therefore, we focus on ratios of cumulants,

$$\frac{C_2}{C_1} = \frac{\langle \delta N^2 \rangle}{\langle N \rangle} = \frac{\sigma^2}{M}, \quad (1.13)$$

$$\frac{C_3}{C_2} = \frac{\langle \delta N^3 \rangle}{\langle \delta N^2 \rangle} = S\sigma, \quad (1.14)$$

$$\frac{C_4}{C_2} = \frac{\langle \delta N^4 \rangle}{\langle \delta N^2 \rangle} - 3 \langle \delta N^2 \rangle = \kappa\sigma^2. \quad (1.15)$$

From the above equations, we can calculate the cumulants and cumulant ratios of the measured net-proton, net-baryon, and net-charge distributions.

1.4 Hadron Resonance Gas Model

One model used to study the QCD phase transition and critical point is the Hadron Resonance Gas (HRG) model. Event-by-event fluctuations of the cumulant ratio of the baryon number are investigated. They used the Boltzmann approximation to calculate the ratio of baryon number susceptibility. Event-by-event fluctuations of the cumulant ratio of baryon number are investigated. They used the Boltzmann approximation to calculate the ratio of baryon number susceptibility. finally, they got the results of the ratio of baryon number susceptibility (related to cumulant ratios), $\frac{\chi_B^{(3)}}{\chi_B^{(2)}} = S\sigma = \tanh(\mu_B/T)$ and $\frac{\chi_B^{(4)}}{\chi_B^{(2)}} = \kappa\sigma^2 = 1$. This result is usually used as a baseline for the study of fluctuations of conserved quantities to find the signature of the QCD phase transition and critical point in heavy-ion collisions.

1.5 σ Field Model

The calculation of the σ field model (Stephanov, 2011) described the behavior of fluctuations of kurtosis (fourth order cumulants) near the QCD critical point. It is realized by the fluctuations of the order parameter σ field,

which can be characterized by the probability distribution as

$$P[\sigma] \sim \exp\{-\Omega[\sigma]/T\}, \quad (1.16)$$

where Ω is the effective action functional for σ field can be augmented in power of σ as

$$\Omega = \int d^3x \left[\frac{(\nabla\sigma)^2}{2} + \frac{m_\sigma^2}{2}\sigma^2 + \frac{\lambda_3}{3}\sigma^3 + \frac{\lambda_4}{4}\sigma^4 + \dots \right]. \quad (1.17)$$

From calculating the 2-point correlation, $\langle\sigma(x)\sigma(0)\rangle$ they found that the correlation length $\xi = 1/m_\sigma$. At $\xi \rightarrow \infty$ is characterized as the critical point in the QCD structure. For zero momentum mode correlation functions, $\sigma_V = \int \sigma(x)d^3x$ in a volume system. Therefore, it can be demonstrated that

$$\langle\sigma_V^2\rangle = VT\xi^2, \quad (1.18)$$

$$\langle\sigma_V^3\rangle = 2\lambda_3VT\xi^6, \quad (1.19)$$

$$\langle\sigma_V^4\rangle = 6VT^3 [2(\lambda_3\xi)^2 - \lambda_4] \xi^8 \equiv \langle\sigma_V^4\rangle - 3\langle\sigma_V^2\rangle^2. \quad (1.20)$$

It is found that the higher order cumulants diverge with ξ faster. Therefore, the negative fourth order cumulants are sensitive signatures of the critical point. In the left panels of Figure 1.3 is the QCD phase diagram from calculation of the sigma field, where the dashed line indicates the chemical freeze-out lines from the critical point to the crossover size. The probability distributions of the σ field demonstrate the fourth order cumulants changed from zero to negative (it is shown in the red region) and to positive (it is shown in the blue region). It leads to a non-monotonic energy dependence of distribution of fourth order cumulants, as shown in right panels of Figure 1.3. It is expected that there is a similar behavior in the $K\sigma^2$ of the net-baryon number as a function of energies.

1.6 STAR experiment

The STAR experiment at RHIC (Abdallah et al., 2021) calculated energy dependence of the cumulant ratios of the net-proton distributions for $0 - 5\%$

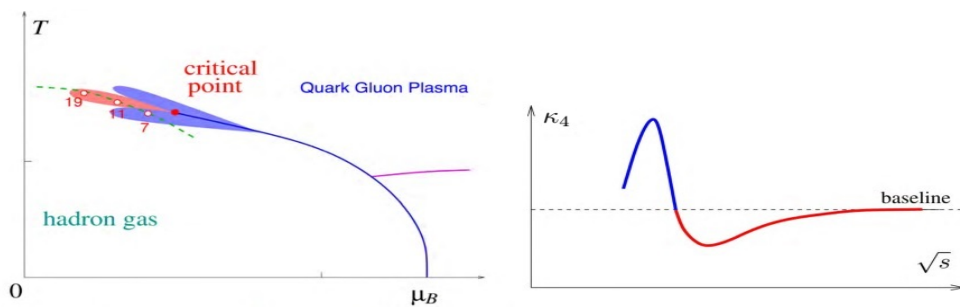


Figure 1.3 Left: the QCD phase diagram from the σ field model. Right: A non-monotonic energy dependence of the distribution of fourth order cumulants ($\kappa_4 = \langle (\delta N)^4 \rangle_c / \langle N \rangle$) (Luo and Xu, 2017).

central Au+Au collisions at $\sqrt{s_{NN}} = 7.7$ to 200 GeV and compared with HRG and UrQMD models. It is found that the STAR experiment results for C_2/C_1 and C_3/C_2 of net-proton distributions show a monotonic behavior with energies. As well, the results from the UrQMD and HRG models show monotonic behavior in the cumulant ratios with energies. On the other hand, the STAR experiment results for the C_4/C_2 of net-proton shows a non-monotonic behavior with energies. Therefore, the STAR experiment explores the critical point at the QCD phase diagram via net-proton multiplicity distributions by using the dependence of the cumulants and cumulant ratios on collision energies, centrality, rapidity, and transverse momentum acceptance.

1.7 Research objectives

1. To study the dependence of cumulant ratios of the net-proton number on the centrality definition.
2. To study the rapidity and transverse momentum acceptance dependence of cumulant ratios of net-proton number on centrality definition.
3. To study the deuteron production at various beam energies and system sizes.

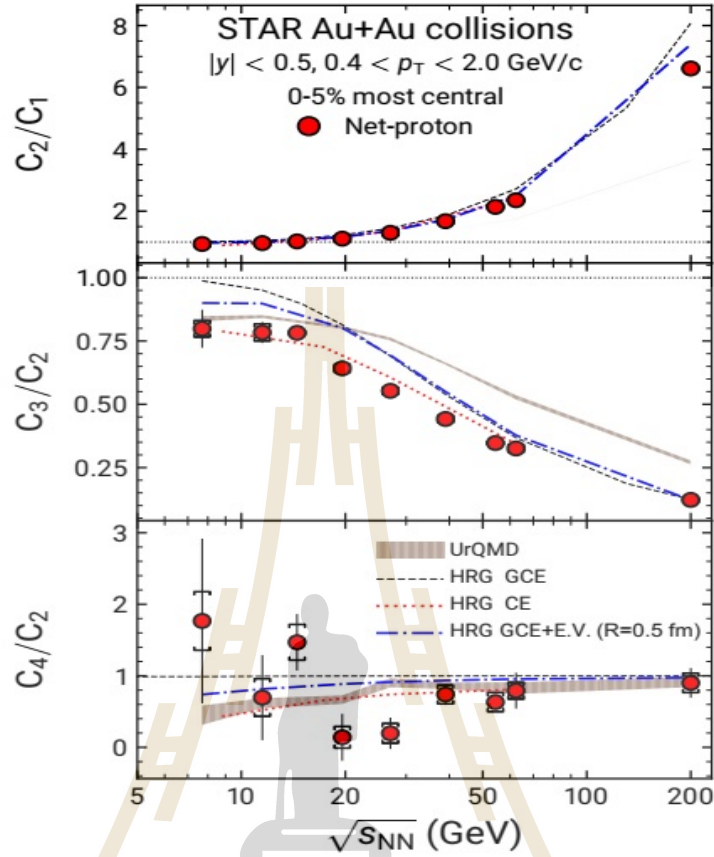


Figure 1.4 Energy dependence of cumulant ratios of the net-proton distributions for 0 – 5% central Au+Au collisions at $\sqrt{s_{NN}} = 7.7$ to 200 GeV and compared with the HRG and UrQMD models.

1.8 Scope and limitations of the study

In my thesis, the fluctuations of the cumulant ratios of the net-proton number on the centrality definition will be measured with Au+Au collisions at the center of mass energy $\sqrt{s_{NN}} = 7.7$ GeV by using the UrQMD model. Moreover, We observe the production of deuteron via phase-space coalescence in the UrQMD model.

CHAPTER II

THE MODEL AND THEORY

2.1 The UrQMD model

The UrQMD model is the ultrarelativistic quantum molecular dynamics model (Bass et al., 1998; Bleicher et al., 1999)(Bass et al., 1998; Bleicher et al., 1999), which is used to study cumulant ratios of net-proton number and deuteron production. The UrQMD model is a transport model for the simulation of p+p, p+A and A+A collisions with range of energy from SIS energy ($\sqrt{s_{NN}} = 2$ GeV) to LHC energy ($\sqrt{s_{NN}} = 14$ TeV). It is based on binary elastic and inelastic scattering of hadrons, including resonance excitation and decays as well as string dynamics. This model has been described in heavy ion collisions from the initiation of the projectile and target nuclei until the end of the final state of the system. The UrQMD model has been used to predict and interpret experimental data at various energies and reaction systems such as: hadron yields, collective flow, hadron resonance production and event-by-event fluctuations.

In this section, we briefly describe the projectile and target nuclei initialization, the equation of motions, cross section of hadron-hadron interactions, and reaction channel in the UrQMD model.

2.1.1 Initialization

In the UrQMD model, The nucleons are expressed by Gaussian shaped density distributions,

$$\varphi_j(\vec{x}_j, t) = \left(\frac{2\alpha}{\pi}\right)^{\frac{3}{4}} \exp\left\{-\alpha(\vec{x}_j - \vec{r}_j(t))^2 + \frac{i}{\hbar}\vec{p}(t)\vec{x}_j\right\}. \quad (2.1)$$

The wave function of the nucleus is defined as the product of the wave functions of the individual nucleons,

$$\Phi = \prod_j \varphi_j(\vec{x}_i, \vec{p}_i, t). \quad (2.2)$$

Each initialized nucleus must meet the aforementioned constraints,

- $\sum_i \vec{q}_i = 0$, which indicates that it is centered in configuration space around 0,
- $\sum_i \vec{v}_i = 0$, indicating that the nucleus is at rest,
- Its binding energy must correspond to the value specified by the Bethe-Weizacker formula,
- The nuclear radius must produce the following mass dependence

$$R(A) \sim r_0 \cdot A^{\frac{1}{3}} \quad (2.3)$$

and have an acceptable surface thickness,

- The nucleus should have a ground state density of nucleus matter at its center. The Gaussian centroids are distributed at random within a spherical configuration space. Due to the finite breadth of the Gaussians, there is a surface region that exceeds the radius of the sphere. Therefore, the radius is reduced by half a layer of nucleons relative to the value given by Equation (2.3).

$$R(A) = r_0 \left(\frac{1}{2} \left[A + \left(A^{\frac{1}{3}} - 1 \right)^3 \right] \right)^{\frac{1}{3}}. \quad (2.4)$$

where the r_0 is radius and is expressed as a function of the nuclear matter ground state density (ρ_0),

$$r_0 = \left(\frac{3}{4\pi\rho_0} \right)^{\frac{1}{3}}, \quad (2.5)$$

The initial nucleon momenta are randomly selected from a distribution between 0 and the local Thomas-Fermi momentum.

$$p_F^{\max} = \hbar c (3\pi^2 \rho)^{\frac{1}{3}}, \quad (2.6)$$

where ρ_0 is the corresponding local proton density or neutron density.

2.1.2 Equation of motion

This section describes the interaction between nucleons in the UrQMD model. The interaction is based on a density-dependent non-relativistic Skyrme-type equation of state with additional Coulomb- and Yukawa potentials. There is no use of momentum-dependent potentials, but the Pauli potential may be included if desired. From Equation (2.1), the nucleon density can be obtained,

$$\varrho_j(\vec{x}_j, t) = \left(\frac{2\alpha}{\pi} \right)^{\frac{3}{2}} \exp \left\{ -2\alpha(\vec{x}_j - \vec{r}_j(t))^2 \right\}, \quad (2.7)$$

In the given context, \vec{x}_j denotes the quantum mechanical position variable, while $\vec{r}_j(t)$ represents the classical Gaussian parameter. The Skyrme-Potential, which disregards momentum dependence and spin exchange, is as follows:

$$V^{sk} = \frac{1}{2!} t_1 \sum_{j,k} \delta(\vec{x}_j - \vec{x}_k) + \frac{1}{3!} t_2 \sum_{j,k} \delta(\vec{x}_j - \vec{x}_k) \delta(\vec{x}_j - \vec{x}_k). \quad (2.8)$$

In order to prevent self-interactions, any primed summation elements consisting of at least two identical indices are omitted. The Skyrme potential is the sum of two-body interaction terms and three-body interaction terms. Because of the linear density dependence of the two-body term, the long-range attractive component of the nucleon-nucleon interaction can be described. The three-body term, whose density dependence is quadratic, is accountable for the short-range repulsive portion of the interaction. Using Equation (2.1) as the wave function of the nucleon, we can calculate the two-body Skyrme potential of particle j as follows,

$$\begin{aligned} V_j^{sk2} &= \sum_k^N \int d\vec{x}_j d\vec{x}_k \varphi_j^*(\vec{x}_j) \varphi_k^*(\vec{x}_k) t_1 \delta(\vec{x}_j - \vec{x}_k) \varphi_j(\vec{x}_j) \varphi_k(\vec{x}_k) \\ &= t_1 \sum_k^N \left(\frac{\alpha}{\pi} \right)^{\frac{3}{2}} \exp \left\{ -\alpha(\vec{r}_j - \vec{r}_k)^2 \right\} \\ &= t_1 \varrho_j^{\text{int}}(\vec{r}_j). \end{aligned} \quad (2.9)$$

The interaction density proposed in the last line of Equation (2.9). This density has the same form as Equation (2.7), which is derived from the Wigner-transform of the Gaussian (2.1), with the exception that the nucleon at location j is neglected and its Gaussian has twice the width of the one used in Equation (2.9). Obtaining the three-body potential of particle j is possible,

$$\begin{aligned}
V_j^{Sk3} &= \frac{1}{2!} \sum_{kl}^N \int d\vec{x}_j d\vec{x}_k d\vec{x}_l \varphi_j^*(\vec{x}_j) \varphi_k^*(\vec{x}_k) \varphi_l^*(\vec{x}_l) \\
&\quad \times t_2 \delta(\vec{x}_j - \vec{x}_k) \delta(\vec{x}_j - \vec{x}_l) \varphi_j(\vec{x}_j) \varphi_k(\vec{x}_k) \varphi_l(\vec{x}_l) \\
&= t_1 \frac{1}{2!} \sum_{kl}^N \left(\frac{4\alpha^2}{3\pi^2} \right)^{\frac{3}{2}} \\
&\quad \times \exp \left\{ -\frac{2}{3} \alpha (\vec{r}_j - \vec{r}_k)^2 + (\vec{r}_k - \vec{r}_l)^2 + (\vec{r}_l - \vec{r}_j)^2 \right\}. \tag{2.10}
\end{aligned}$$

When infinite nuclear matter is involved, this potential is considered when the individual relative distances are close to their average value. Thus, the relative distance between particles k and l can be replaced by the average of the other two relative distances,

$$V_j^{Sk3} \approx \frac{1}{2!} t_2 \sum_{kl}^N \left(\frac{4\alpha^2}{3\pi^2} \right)^{\frac{3}{2}} \exp \left\{ -\alpha (\vec{r}_j - \vec{r}_k)^2 + (\vec{r}_k - \vec{r}_l)^2 \right\}. \tag{2.11}$$

By utilizing the definition of the interaction-density provided in Equation (2.10), Equation (2.11) can be expressed as Equation (2.12),

$$V_j^{Sk3} \approx t_2 3^{-\frac{3}{2}} (\rho_j^{\text{int}})^2 \rightarrow t_\gamma (\gamma + 1)^{-\frac{3}{2}} (\rho_j^{\text{int}})^\gamma. \tag{2.12}$$

It is worth noting that the expression in Equation (2.12) is always used for the UrQMD model, even in cases where $\gamma = 2$

Equations (2.14), (2.15), and (2.16), respectively, describe the Yukawa, Coulomb, and (optional) Pauli potentials. They take the form of interactions between two

particles,

$$\begin{aligned}
 V_{\text{Yuk}}^{ij} &= V_0^{\text{Yuk}} \frac{\exp\{-|\vec{r}_i - \vec{r}_j|/\gamma_Y\}}{|\vec{r}_i - \vec{r}_j|}, \\
 V_{\text{Coul}}^{ij} &= \frac{Z_i Z_j e^2}{|\vec{r}_i - \vec{r}_j|}, \\
 V_{\text{Pau}}^{ij} &= V_{\text{Pau}}^0 \left(\frac{\hbar}{q_0 p_0} \right)^3 \exp \left\{ -\frac{|\vec{r}_i - \vec{r}_j|^2}{2q_0^2} - \frac{|\vec{p}_i - \vec{p}_j|^2}{2p_0^2} \right\} \delta_{\tau_i \tau_j} \delta_{\sigma_i \sigma_j},
 \end{aligned} \tag{2.13}$$

where σ_j and τ_j are the spin and isospin of particle j , Z_j denotes its charge. In the case of infinite nuclear matter, the Yukawa potential contribution to total energy has the same linear density dependence as the two-body Skyrme contribution. Consequently, all parameter sets satisfying the following relation for the parameter t_1 would produce the same equation of state for infinite nuclear matter,

$$\frac{1}{2} t_1 + 2\pi V_0^{\text{Yuk}} \gamma_Y^2 = \text{const.} \tag{2.14}$$

In finite nuclei, it is possible to adjust the parameters of the Yukawa potential to achieve the appropriate surface properties of the nuclei without changing the equation of state.

The classical Hamiltonian in UrQMD is responsible for governing the motion of parameters \vec{r}_j and \vec{p}_j of the wave-functions, can be defined by

$$\begin{aligned}
 H_{\text{UrQMD}} &= \sum_{j=1}^N E_j^{\text{kin}} + \frac{1}{2} \sum_{j=1}^N \sum_{k=1}^N \left(E_{jk}^{\text{Sk2}} + E_{jk}^{\text{Yukawa}} + E_{jk}^{\text{Coulomb}} + E_{jk}^{\text{Pauli}} \right) \\
 &\quad + \frac{1}{6} \sum_{j=1}^N \sum_{k=1}^N \sum_{l=1}^N E_{jkl}^{\text{Sk3}}
 \end{aligned} \tag{2.15}$$

where the kinetics term is

$$E_j^{\text{kin}} = \sqrt{p_j^2 + m_j^2}, \tag{2.16}$$

and the two body Skyrme is

$$E_{jk}^{\text{Sk2}} = t_1 \left(\frac{\alpha}{\pi} \right)^{\frac{3}{2}} \exp \{ -\alpha r_{jk}^2 \}, \tag{2.17}$$

and the three body Skyrme is

$$E_{jkl}^{\text{Sk3}} = t_\gamma \left(\frac{4\alpha^2}{3\pi^2} \right)^{\frac{3}{2}} \exp \left\{ -\alpha (r_{jk}^2 + r_{jl}^2) \right\}. \quad (2.18)$$

The Yukawa potential is

$$E_{jk}^{\text{Yukawa}} = v_0^{\text{Yuk}} \frac{1}{2r_{jk}} \exp \left\{ \frac{1}{4\alpha\gamma^2} \right\} \times \left[\exp \left\{ -\frac{r_{jk}}{\gamma_Y} \right\} \left(1 - \operatorname{erf} \left(\frac{1}{2\gamma_Y\sqrt{\alpha}} - \sqrt{\alpha}r_{jk} \right) \right) - \exp \left\{ \frac{r_{jk}}{\gamma_Y} \right\} \left(1 - \operatorname{erf} \left(\frac{1}{2\gamma_Y\sqrt{\alpha}} + \sqrt{\alpha}r_{jk} \right) \right) \right], \quad (2.19)$$

and the Coulomb potential is

$$E_{jk}^{\text{Coulomb}} = \frac{Z_i Z_j e^2}{r_{jk}} \operatorname{erf} \left(\sqrt{\alpha} r_{jk} \right), \quad (2.20)$$

and the Pauli potential is

$$E_{jk}^{\text{Pauli}} = v_{\text{Pau}}^0 \left(\frac{\hbar}{p_0 q_0} \right)^3 \left(1 - \frac{1}{2\alpha q_0^2} \right)^{-\frac{3}{2}} \times \exp \left\{ -\frac{\alpha r_{jk}^2}{2\alpha q_0^2 + 1} - \frac{p_{jk}^2}{2p_0^2} \right\} \delta_{\tau_j \tau_k} \delta_{\sigma_j \sigma_k}, \quad (2.21)$$

with

$$r_{jk} = |\vec{r}_j - \vec{r}_k| \quad (2.22)$$

and

$$p_{jk} = |\vec{p}_j - \vec{p}_k|. \quad (2.23)$$

In Table 2.1 shows the parameters for achieving only a hard equation of state for the UrQMD model. These potential interactions are imposed for particles with relative momenta $\Delta p < 2 \text{ GeV}/c$. For the hadronic collision the potential interactions are neglected with $\Delta p > 2 \text{ GeV}/c$.

2.1.3 Cross section of hadron-hadron interactions

The particle species and energy dependent cross-sections of hadron-hadron interactions are fundamental inputs in the microscopic transport models

Table 2.1 With and without the Pauli potential, the parameters for implementing the rigid equation of state in the UrQMD model are listed below.

parameter	without Pauli-potential	with Pauli-potential
$\alpha(\text{fm}^{-2})$	0.25	0.1152
$t_1(\text{MeVfm}^2)$	-7264.04	-84.5
$t_\gamma(\text{MeVfm}^6)$	87.65	188.2
γ	1.675	1.46
$V_0^{\text{Yukawa}}(\text{MeVfm})$	-0.498	-85.1
γ_Y	1.4	1.0
$V_0^{\text{Pauli}}(\text{MeV})$	-	98.95
$q_0(\text{fm})$	-	2.16
$p_0(\text{MeV}/c)$	-	120

and thus crucial for the UrQMD model. The total cross-sections are interpreted geometrically. The collision between two hadrons will occur when

$$d < \sqrt{\frac{\sigma_{\text{tot}}}{\pi}}, \quad (2.24)$$

where d is the distance between two hadrons and σ_{tot} are the total cross section of the two hadrons.

In UrQMD model, the total cross section is dependent the spin of the colliding particles and the center of mass energy. The UrQMD model's cross sections are compared with experimental data.

In this model, there are 55 baryon and 32 meson species, as well as all resonances with masses up to 2.25 GeV. Table 2.2 displays the baryons and baryon resonances that can be occupied in UrQMD. In addition, Table 2.3 presents mesons and meson resonances ordered according to their spin and parity.

Table 2.2 ID of baryon and baryon-resonances used in UrQMD model.

ID	Nucleon	ID	Delta	ID	Lambda	ID	Sigma	ID	Xi	ID	Omega
1	N ₉₈₃	17	Δ_{1232}	27	Λ_{1116}	40	Σ_{1192}	49	Ξ_{1317}	55	Ω_{1671}
2	N ₁₁₄₀	18	Δ_{1600}	28	Λ_{1405}	41	Σ_{1385}	50	Ξ_{1530}		
3	N ₁₅₂₀	19	Δ_{1620}	29	Λ_{1520}	42	Σ_{1660}	51	Ξ_{1690}		
4	N ₁₅₃₅	20	Δ_{1700}	30	Λ_{1600}	43	Σ_{1670}	52	Ξ_{1820}		
5	N ₁₆₅₀	21	Δ_{1900}	31	Λ_{1670}	44	Σ_{1775}	53	Ξ_{1950}		
6	N ₁₆₇₅	22	Δ_{1905}	32	Λ_{1690}	45	Σ_{1790}	54	Ξ_{2025}		
7	N ₁₆₈₀	23	Δ_{1910}	33	Λ_{1800}	46	Σ_{1915}				
8	N ₁₇₀₀	24	Δ_{1920}	34	Λ_{1810}	47	Σ_{1940}				
9	N ₁₇₁₀	25	Δ_{1930}	35	Λ_{1820}	48	Σ_{2030}				
10	N ₁₇₂₀	26	Δ_{1950}	36	Λ_{1830}						
11	N ₁₉₀₀			37	Λ_{1890}						
12	N ₁₉₉₀			38	Λ_{2100}						
13	N ₂₀₈₀			39	Λ_{2110}						
14	N ₂₁₉₀										
15	N ₂₂₀₀										
16	N ₂₂₅₀										

Cross-Section of Baryon-Baryon Reaction

The formula for the total cross-section of the baryon-baryon reaction $A + C \rightarrow D + E$ is

$$\sigma_{\text{tot}}^{\text{BB}}(\sqrt{s}) \propto (2S_D + 1)(2S_E + 1) \frac{\langle p_{D,E} \rangle}{\langle p_{A,C} \rangle} \frac{1}{s} |\mathcal{M}(D, E)|^2, \quad (2.25)$$

where S_i is the spin of particle, \mathcal{M}^2 is the matrix element which is a function of masses of outgoing particle (D,E) and $\langle p_{i,j} \rangle$ are the moments of the pairs of particles in the two particle restframe. It can be defined as

$$\langle p_{i,j}(\sqrt{s}) \rangle = \frac{1}{2\sqrt{s}} \sqrt{(s - (m_i + m_j)^2)(s - (m_i - m_j)^2)}. \quad (2.26)$$

Table 2.3 Mesons and meson resonance are arranged in the UrQMD model in accordance with spin and parity.

ID	0^{-+}	ID	1^{--}	ID	0^{++}	ID	1^{++}
101	π	104	K^*	111	a_0	114	a_1
106	K	108	ω	110	K_0^*	113	K_1^*
102	η	103	ρ	105	f_0	115	f_1
107	η'	109	ϕ	112	f_0^*	116	f_0'

ID	1^{+-}	ID	2^{++}	ID	$(1^{--})^*$	ID	$(1^{--})^*$
122	b_1	118	a_2	126	ρ_{1450}	130	ρ_{1700}
121	1	117	K_2^*	125	K_{1410}^*	129	K_{1680}^*
123	h_1	119	f_2	127	ω_{1420}	131	ω_{1662}
124	f_1'	120	f_2'	128	ϕ_{1680}	132	ϕ_{1900}

The baryon-baryon cross sections is compared in detail between the UrQMD model and experiment data (Zyla et al., 2020) can be examined in Bleicher: 1999xi.

Cross-Section of Antibaryon-Baryon Reactions

The energies at $p_{\text{lab}} \leq 100$ GeV/c is important to the total cross-section which originates the process of annihilation. The earlier experiments of $\bar{p}p$ annihilation indicated a number of differences from the non-annihilation channels, but it is not obviously understood whether these differences come from the kinematic restrictions on the available phase space or whether they are associated with dynamical differences between the annihilation and non-annihilation mechanisms. By comparing pp and non-annihilation pp interactions at 32 GeV/c, the experimental outcomes are presented by (Zabrodin et al., 1995).

The UrQMD model uses available data to set the elementary annihilation cross section. Figure 2.1 shows a comparison between the UrQMD parameterization and the data for the total, elastic, and annihilation cross sections of $\bar{p}p$. The solid line represents the total $\bar{p}p$ cross sections, the dashed line represents the annihilation cross sections, and the dotted line represents the elastic cross

sections. For the annihilation cross section is proposed by Koch and Dover

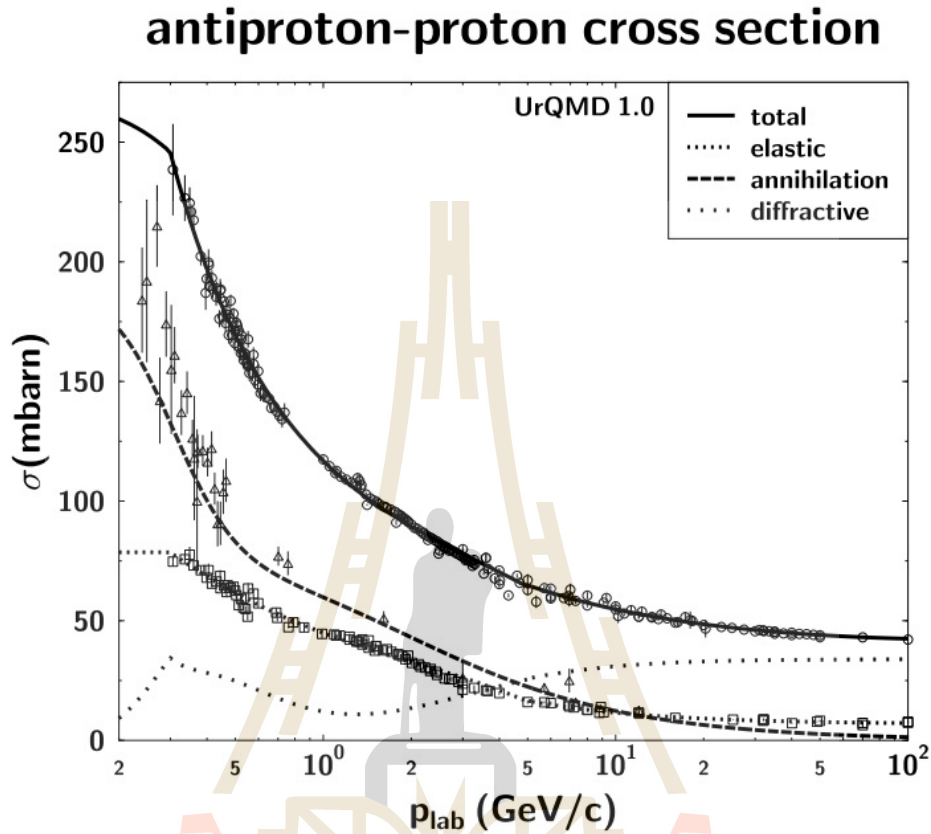


Figure 2.1 The UrQMD parameterization of $\bar{p}p$ cross sections compared with experiment data (Barnett et al., 1996) The diffractive cross section is the difference between the total cross section and the sum of elastic and annihilation cross sections.

(Koch and Dover, 1989)

$$\sigma_{\text{ann}}^{\bar{p}p} = \sigma_0^N \frac{s_0}{s} \left[\frac{A^2 s_0}{(s - s_0)^2 + A^2 s_0} + B \right], \quad (2.27)$$

with $\sigma_0^N = 120$ mb, $s_0 = 4m_N^2$, $A = 50$ MeV and $B = 0.6$.

The total and elastic cross sections of $\bar{p}p$ reactions are considered according to the CERN/HERA parameter as

$$\sigma(p) = A + Bp^n + C\ln^2(p) + D\ln(p), \quad (2.28)$$

where p indicates the laboratory-momentum in GeV/c, σ indicates the cross-section in millibarn (mb). The respective parameters are shown in Table 2.4.

Table 2.4 The CERN/HERA parameterization parameters for the elastic and total cross sections of $\bar{p}p$. This parameters is used in UrQMD for $p_{\text{lab}} > 5$ GeV/c

σ	A	B	C	D	n
total	38.4	77.6	0.26	-1.2	-0.64
elastic	10.2	52.7	0.125	-1.28	-1.16

For $p_{\text{lab}} > 5$ GeV/c, The UrQMD model employs a different parameterization to calculate the total and elastic cross sections, which are shown in Equations (2.29) and (2.30), respectively

$$\sigma_{\text{tot}}(p) = \begin{cases} 75.0 + 43.1p^{-1} + 2.6p^{-2} - 3.9p & : 0.3 < p < 5 \\ 271.6 \exp(-1.1p^2) & : p < 0.3 \end{cases} \quad (2.29)$$

$$\sigma_{\text{el}}(p) = \begin{cases} 31.6 + 18.3p^{-1} - 1.1p^{-2} - 3.8p & : 0.3 < p < 5 \\ 78.6 & : p < 0.3 \end{cases} \quad (2.30)$$

Experimentally, the total cross-section is greater than the sum of the annihilation and elastic cross-sections,

$$\Delta\sigma = \sigma_{\text{tot}} - \sigma_{\text{el}} - \sigma_{\text{ann}} \quad (2.31)$$

In UrQMD, $\Delta\sigma$ is the diffractive cross-section that characterizes the probability of exciting one or more of the colliding particles to a resonance or string state.

Cross section of Meson-meson and meson-baryon Reactions

At center-of-mass energies up to 2.2 GeV, resonance scattering, or the formation of intermediate resonance, dominates the meson-baryon and meson-meson interactions. The total meson-baryon cross section for non-strange

particles can be expressed as follows,

$$\begin{aligned} \sigma_{\text{tot}}^{\text{MB}}(\sqrt{s}) = & \sum_{R=\Delta, N^*} \langle j_B, m_B, j_M, m_M \parallel J_R, M_R \rangle \\ & \times \frac{2S_R+1}{(2S_B+1)(2S_M+1)} \\ & \times \frac{\pi}{p_{\text{cm}}^2} \frac{\Gamma_{R \rightarrow \text{MB}} \Gamma_{\text{tot}}}{(M_R - \sqrt{s})^2 + \Gamma_{\text{tot}}^2/4}. \end{aligned} \quad (2.32)$$

The total width of decay (Γ_{tot}) is the sum of all partial widths of decay. It's contingent on the mass of the excited resonance. $\Gamma_{R \rightarrow \text{MB}}$ is the partial width of decay into the exit channel for two particles, and M_R is the resonance pole mass. The data of the partial decay widths and all pole masses are given in (Zyla et al., 2020).

We investigate the collisions of strange baryons and mesons. These UrQMD processes are contrasted with experimental data (?). Figure 2.2 shows the cross section of K^- on proton interactions as a function of laboratory momentum (p_{lab}). The formation of hyperon resonances is observed to be readily apparent at lower energies, whereas the t-channel reaction dominates the high energy tail. In addition, the K^+ on protons cross section is shown in Figure 2.3. It was determined that the formation of resonances is forbidden because the s-quark cannot be destroyed by non-strange baryons. The elastic channel and the t-channel excitation of both particles are used. The CERN-HERA parameters determine the cross sections at very high energies. The additive quark model is utilized to describe the total meson-meson cross-sections.

2.1.4 The Additive Quark Model (AQM)

The Additive Quark Model (AQM) is used to calculate the indeterminate cross sections (Close, 1979; Perkins, 1982). To apply the AQM to calculations of heavy ion collisions, the cross sections of quark interactions must be determined, which can be approximated using the masses of quarks. The unknown total cross section is then calculated based on the assumption that the s quark has a 40% smaller cross section than the u and d particles. Regge theory (Goulianos, 1983) produces the elastic cross-section.

$$\sigma_{\text{elastic}} = 0.039 \sigma_{\text{total}}^{\frac{3}{2}} [\text{mb}], \quad (2.33)$$

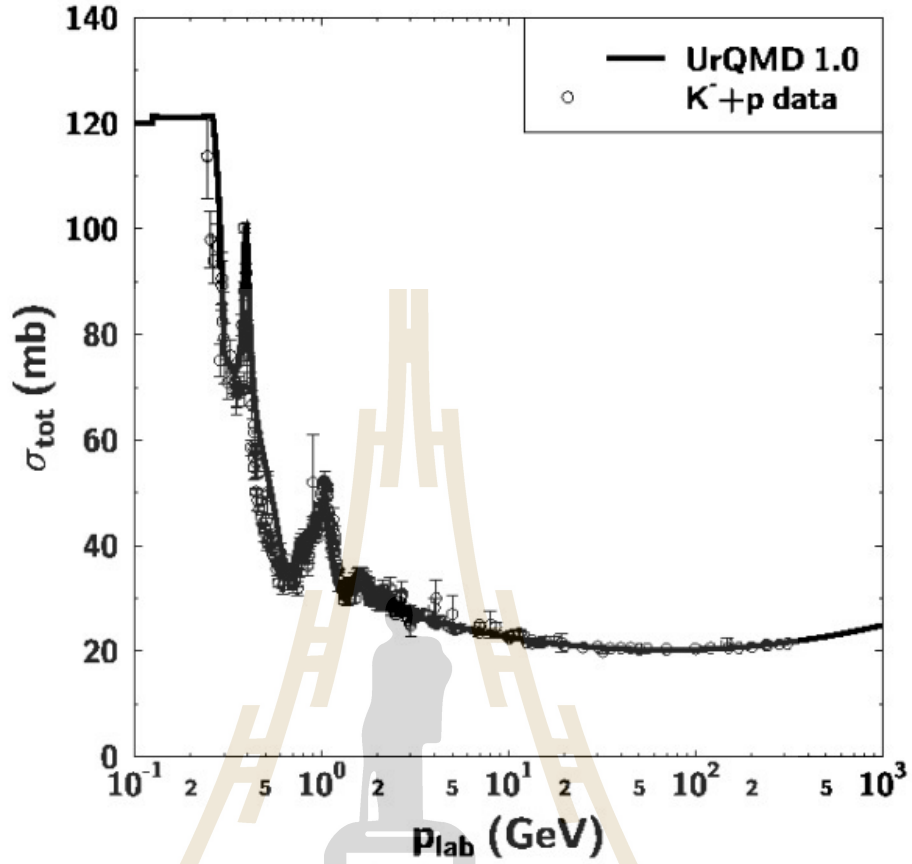


Figure 2.2 The total cross-section of $K^- p$ interaction as a function of laboratory momentum (p_{lab}). The data are taken from (Zyla et al., 2020).

where

$$\sigma_{\text{total}} = 40 \left(\frac{2}{3} \right)^{m_1+m_2} \left(1 - 0.4 \frac{s_1}{3 - m_1} \right) \left(1 - 0.4 \frac{s_2}{3 - m_2} \right) [\text{mb}], \quad (2.34)$$

Due to the interactions' high energy, there is no distinction between particles and antiparticles. The cross-sections of non-strange baryons are not calculated via the AQM because they have an obvious energy dependence in line with experimental data. The Cross-sections of meson-baryon and meson-meson interactions are expressed by

$$\sigma_{X_1 X_2}(\sqrt{s}) = \frac{\sigma_{\pi N}(\sqrt{s})}{\sigma_{\pi N}^{\text{AQM}}} \sigma_{X_1 X_2}^{\text{AQM}} \quad (2.35)$$

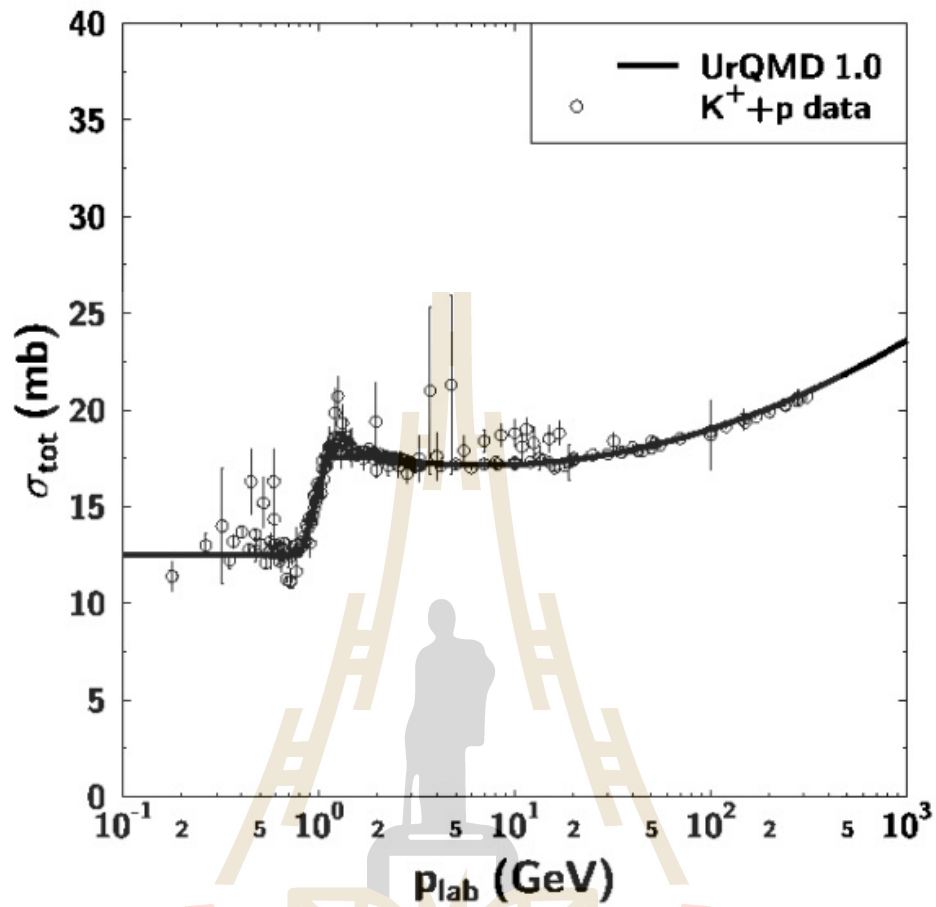


Figure 2.3 The total cross-section of K^+p interaction as a function of laboratory momentum (p_{lab}). The data are taken from (Zyla et al., 2020).

The total cross-sections of interaction of baryon-baryon, meson-baryon, and meson-meson is calculated in Tables 2.5, 2.6, and 2.7, respectively.

Table 2.5 The cross section of baryon-baryon reactions in [mb] according to the Additive Quark Model. The baryon-baryon scattering is demonstrated explicitly.

$B_1 B_2$	N	Λ	Ξ	Ω
N	40.0	34.7	29.3	24.0
Λ	34.7	30.0	25.4	20.8
Ξ	29.3	25.4	21.5	17.8
Ω	24.0	20.8	17.6	14.4

Table 2.6 The cross-section of meson-bayron reactions in [mb] according to the Additive Quark Model. The meson-bayron scattering in the resonance region ($\sqrt{s} < 1.7$ GeV) is demonstrated explicitly.

M_1B_2	N	Λ	Ξ	Ω
π	26.6	23.1	19.6	16.0
K	21.3	18.5	15.6	12.8
Φ	16.0	13.9	11.7	9.6

Table 2.7 The cross-sections of meson-meson reactions in [mb] according to the Additive Quark Model. The meson-meson scattering in the resonance region ($\sqrt{s} < 1.7$ GeV) is demonstrated explicitly.

M_1M_2	π	K	Φ
π	17.8	14.2	10.7
K	14.2	11.4	8.5
Φ	10.7	8.5	6.4

2.1.5 Reaction channel

Particle production primarily takes place via the production and decay of resonances at energies below $\sqrt{s} = 5$ GeV for baryon-baryon interactions and $\sqrt{s} = 3$ GeV for meson-baryon and meson-meson interactions. Nevertheless, above $\sqrt{s} = 3.5$ GeV, the cross sections are neglected because the multiple decay and string channels are considered and allowed for the production of multiple resonances.

This section focuses on high-energy particle production through baryon-baryon interactions, which primarily occurs via resonances. Furthermore, the string model can also account for the generation of particles in high-energy domains through the mechanism of baryon-antibaryon interaction.

Resonances

Baryon resonances are generated via two distinct processes:

ii) soft production: $\pi^- + p \rightarrow \Delta^0, K^- + p \rightarrow \Lambda^* \dots$

i) hard production: $N + N \rightarrow \Delta N, \Delta\Delta, N^*N, \text{ etc.}$

There are six channels of non-strange resonance excitation for the UrQMD model, i.e. $NN \rightarrow N\Delta_{1232}, NN^*, N\Delta^*, \Delta_{1232}\Delta_{1232}, \Delta_{1232}N^*, \text{ and } \Delta_{1232}\Delta^*$. The Δ_{1232} is explicitly listed, whereas higher excitations of the Δ resonance is denoted as Δ^* . Once the excited resonance numbers have been allocated, it becomes necessary to ascertain its mass and properties. Table 2.8 presents the masses, widths, and branching ratios of non-strange baryon-resonances. The meson-resonances must be seen in Bass:1998ca. Note that the soft production produce strange particles.

Strings

The string model (similar to the LUND model (Andersson et al., 1983)) is used to characterize the inelastic reactions in the high energy regime and baryon-antibaryon annihilation. The string model is based on the assumption that the color field between two quarks or anti-quarks at sufficiently great distances can be transformed into the color string. Between the quark and diquark, the linear string potential is located at z_1 and z_2 , respectively. It could be described as

$$V = \kappa |z_1 - z_2|, \quad (2.36)$$

where κ is the string tension. The lattice QCD calculation (Born et al., 1994) supports this form of potential.

From the Hamiltonian, we obtain the dynamics of the quark system (with p_1 and p_2 as the quark momenta).

$$H = |p_1| + |p_2| + \kappa |z_1 - z_2|, \quad (2.37)$$

which leads to the motion equation for the massless string endpoints,

$$\frac{dp_i}{dt} = -\frac{\partial H}{\partial z_i} = -\text{sign}(z_i - z_i'), \quad (2.38)$$

$$\frac{dz_i}{dt} = +\frac{\partial H}{\partial p_i} = \text{sign}(p_i). \quad (2.39)$$

Table 2.8 Masses (GeV/c^2), widths (MeV) and branching ratios of non-strange baryon-resonances in UrQMD model. All parameters are given by the Review of Particle Properties (Barnett et al., 1996).

resonance	mass	width	$N\gamma$	$N\pi$	$N\eta$	$N\omega$	$N\rho$	$N\pi\pi$	$\Delta_{1232}\pi$	$N_{1440}^*\pi$	Λ_K
N_{1440}^*	1.440	200		0.70				0.05	0.25		
N_{1520}^*	1.520	125		0.60				0.15	0.25		
N_{1535}^*	1.535	150	0.001	0.55	0.35			0.05		0.05	
N_{1650}^*	1.650	150		0.65	0.05			0.05	0.10	0.05	0.10
N_{1675}^*	1.675	140		0.45					0.55		
N_{1680}^*	1.680	120		0.65				0.20	0.15		
N_{1700}^*	1.700	100		0.10	0.05		0.05	0.45	0.35		
N_{1710}^*	1.710	110		0.15	0.20		0.05	0.20	0.20	0.10	0.10
N_{1720}^*	1.720	150		0.15			0.25	0.45	0.10		0.05
N_{1900}^*	1.870	500		0.35		0.55	0.05		0.05		
N_{1990}^*	1.990	550		0.05			0.15	0.25	0.30	0.15	0.10
N_{2080}^*	2.040	250		0.60	0.05		0.25	0.05	0.05		
N_{1440}^*	1.440	200		0.70				0.05	0.25		
N_{1520}^*	1.520	125		0.60				0.15	0.25		
N_{1535}^*	1.535	150	0.001	0.55	0.35			0.05		0.05	
N_{1650}^*	1.650	150		0.65	0.05			0.05	0.10	0.05	0.10
N_{1675}^*	1.675	140		0.45					0.55		
N_{1680}^*	1.680	120		0.65				0.20	0.15		
N_{1700}^*	1.700	100		0.10	0.05		0.05	0.45	0.35		
N_{1710}^*	1.710	110		0.15	0.20		0.05	0.20	0.20	0.10	0.10
N_{1720}^*	1.720	150		0.15			0.25	0.45	0.10		0.05
N_{1900}^*	1.870	500		0.35		0.55	0.05		0.05		
N_{1990}^*	1.990	550		0.05			0.15	0.25	0.30	0.15	0.10
N_{2080}^*	2.040	250		0.60	0.05		0.25	0.05	0.05		
N_{2190}^*	2.190	550		0.35			0.30	0.15	0.15	0.05	
N_{2220}^*	2.220	550		0.35			0.25	0.20	0.20		
N_{2250}^*	2.250	470		0.30			0.25	0.20	0.20	0.05	
Λ_{1232}^*	1.232	115	0.01	1.00							
Λ_{1600}^*	1.700	200		0.15					0.55	0.30	
Λ_{1620}^*	1.675	180		0.25					0.60	0.15	
Λ_{1700}^*	1.750	300		0.20			0.10		0.55	0.15	
Λ_{1900}^*	1.850	240		0.30			0.15		0.30	0.25	
Λ_{1905}^*	1.880	280		0.20			0.60		0.10	0.10	
Λ_{1910}^*	1.900	250		0.35			0.40		0.15	0.10	
Λ_{1920}^*	1.920	150		0.15			0.30		0.30	0.25	
Λ_{1930}^*	1.930	250		0.20			0.25		0.25	0.30	
Λ_{1950}^*	1.950	250	0.01	0.45			0.15		0.20	0.20	

The sign of $\text{sign}(z_i - z_i')$ relates to a change in momentum, whereas the sign of quark momentum p_i defines the propagation direction.

When the momentum transfer is sufficiently high, $q\bar{q}$ pairs are produced from the vacuum and break the string excitation into pieces. In their rest frame, each of the produced $q\bar{q}$ pairs have small relative momenta due to the consistent stretching of the color string. Hadrons produced through string fragmentation will be distributed in a consistent manner within the kinematically allowed range of $y_{\min} = 0$ and $y_{\max} = \ln(s/m_T^2)$.

Figure 2.4 shows the production of particles during string excitation. On the left are showed the quark and diquark (non-strange) with string tension. Afterwards, two quark-antiquark pairs ($u\bar{u}$ and $s\bar{s}$ pair) are created from the vacuum. A diquark and a new s quark can combine to create a hyperon. In addition, a new s quark and an u quark can combine to create a kaon. Finally, a new u quark and a quark at the end of a string can combine to create a pion.



Figure 2.4 Particle production resulting from string excitation.

The probability $|M^2|$ for the creation of a $q\bar{q}$ pair with mass (m) in a color field can be written as,

$$|M^2| = \text{constant} \times \exp\left(-\frac{\pi m^2}{\kappa}\right), \quad (2.40)$$

where the value for κ is 1 GeV/fm. This probability is introduced by Schwinger's QED-based results for particle-antiparticle creation in a strong electric field (Schwinger, 1951). The relative production probabilities of the different quark flavors are adjusted to e^+e^- data:

$$u : d : s : \text{diquark} = 1 : 1 : 0.35 : 0.1. \quad (2.41)$$

To determine which type of hadron is produced based on the quark configuration formed in the color field, we will choose in the case of a produced

- (i) baryon — the baryon decays into the octet and decuplet with equal probabilities.
- (ii) meson — the meson multiplets are determined using a probability proportional to spin degeneracy and inverse mean mass m ,

$$P_{J^{PC}} \sim \frac{2S + 1}{\langle m \rangle_{J^{PC}}} \quad (2.42)$$

Table 2.9 presents the corresponding values for the meson multiplets that are taken into consideration by the UrQMD model.

Table 2.9 Probabilities for the different meson multiplets.

multiplet J^{PC}	0^{-+}	1^{--}	0^{++}	1^{++}	2^{++}	1^{+-}	1^{--*}	1^{--**}
probability	0.102	0.190	0.056	0.124	0.197	0.127	0.110	0.095

A diquark-antidiquark (or quark-antiquark) pair is formed and inserted between the primary constituent diquark-antidiquark (or quark-antiquark) pair during the string's excitation and fragmentation. At the string's endpoints, a hadron is then generated at random. The quark content of the hadron must be determined, including its species and charge. Breit-Wigner distributions determine the mass in the case of resonances. Finally, the fraction of the string's energy designated to the newly created hadron must be determined. After a random transverse momentum is assigned to the hadron, the fragmentation function determines the fraction of momentum transferred from the string to the hadron.

2.2 Cumulants

In statistics, the moments are a quantitative measurement of the shape of a set of the probability density. The moment consists of five moments. The zeroth moment will always be equal to 1, which means that the probability distribution has a normalized mean. The first moment is the mean, which is defined as

$$M = \frac{\sum_{i=1}^N x_i}{N}, \quad (2.43)$$

where x_i is the particle number in event i ,
 N is the number of events.

The second moment is variance, which is a measurement of how much the probability distribution is spread from the mean. The variance is defined as the square of the standard deviation. It can be calculated as follows:

$$\sigma^2 = \frac{\sum_{i=1}^N (x_i - M)^2}{N}. \quad (2.44)$$

The third moment is Skewness, which is a measurement of the asymmetry of a probability distribution. It describes the extent to which a distribution deviates from being symmetric. A distribution is said to be symmetric if it is mirror-image about its mean. If the distribution is skewed, it means that it is not symmetric. The skewness of a distribution can be calculated as follows:

$$S = \frac{\sum_{i=1}^N (x_i - M)^3}{N\sigma^3}. \quad (2.45)$$

The skewness measure indicates the direction and degree of skewness in a distribution. If the skewness measure is positive, the tail of the distribution is longer on the right side, it is called right-skewed or positively skewed. If the skewness measure is negative, the tail of the distribution is longer on the left side, it is called left-skewed or negatively skewed. If the skewness measure is close to zero, the distribution is symmetric. These three types are shown in Figure 2.5.

The fourth moment is Kurtosis, which is a statistical measurement used to describe the shape of a probability distribution. It provides information about the tailedness or peakedness of the distribution in comparison to the normal distribution. It can be calculated as follows:

$$K = \frac{\sum_{i=1}^N (x_i - M)^4}{N\sigma^4} - 3. \quad (2.46)$$

If the data distribution has a higher peak than a normal distribution, it is called leptokurtic or positive kurtosis, while the data distribution has a lower peak than a normal distribution, it is called platykurtic or negative kurtosis. A kurtosis value of 0 indicates a normal distribution. The kurtosis distribution are shown in Figure 2.6.

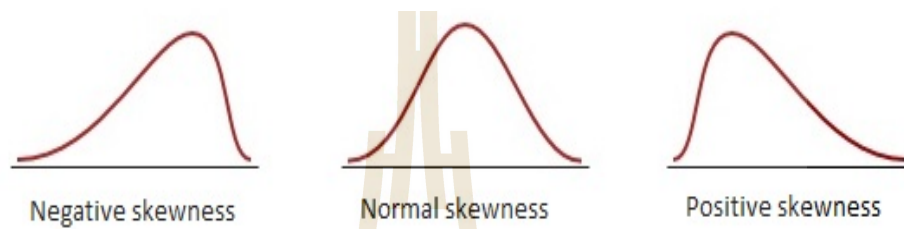


Figure 2.5 Difference of the skewness distribution (Sheskin, 2003).

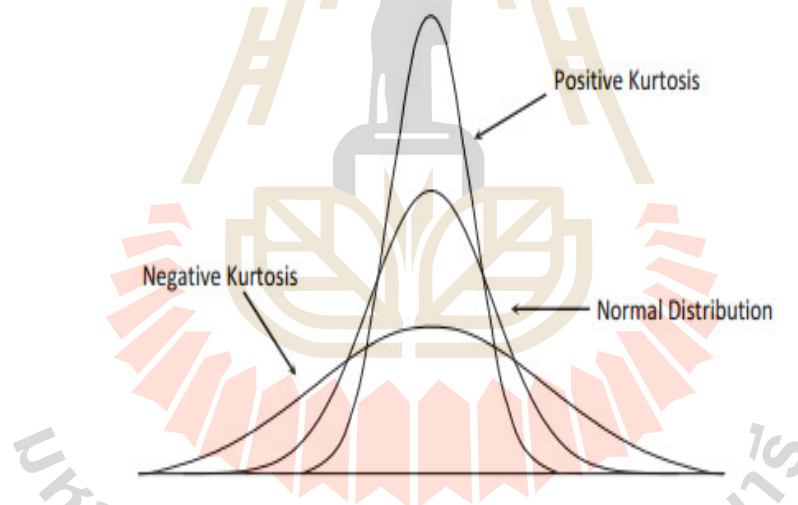


Figure 2.6 Difference of the kurtosis distribution. (Glen, 2017).

2.3 Statistical Error

The statistical error is estimated from delta theorem (Luo, 2012) for normal distributions. The error of the cumulant ratios are expressed by

$$\text{error}\left(\frac{C_r}{C_2}\right) \propto \frac{\sigma^{r-2}}{\sqrt{n}}, \quad (2.47)$$

where r^{th} is the order of cumulants,
 n is the number of events,
 C_2 is the variance (σ^2).

From Equation (15), the error of skewness and kurtosis can be derived as following formula

$$\text{error}(S\sigma) = \frac{\sigma}{\sqrt{n}}, \quad (2.48)$$

$$\text{error}(\kappa\sigma^2) = \frac{\sigma^2}{\sqrt{n}}. \quad (2.49)$$

CHAPTER III

HIGHER ORDER CUMULANTS OF NET-PROTON NUMBER ON THE CENTRALITY DEFINITION

Exploration the QCD phase structure of the strong interaction has been investigated both in experimentally and theoretically. The QCD based models predicted that at large μ_B region, the phase transition of QCD is a first-order and exist the endpoint of the first order phase boundary a so called QCD Critical Point (CP) (Stephanov, 2004). The QCD phase structure is revealed through the study of event-by-event fluctuations of conserved quantities, such as net-baryon (B), net-charge (Q) and net-strangeness (S), which can be determined in the form of cumulants. Especially, the measurement of higher order cumulants of the net-proton number close to the phase transition (Steinheimer and Randrup, 2012; Chomaz et al., 2004; Randrup, 2004; Sasaki et al., 2007) and CP (Stephanov et al., 1998; Stephanov, 2009; Koch, 2010).

Although higher order cumulants are widely measured, it is still difficult to obtain a detailed understanding and interpretation of the measured higher order cumulants due to uncertainties in the centrality definition, the dependence of transverse momentum (p_T) and rapidity acceptance, and detector efficiency. Therefore, In this section, the UrQMD model is used to elucidate some of the previously mentioned effects and their influence on distribution of net-proton cumulant ratios.

3.1 Centrality Definition

In nucleus-nucleus collisions, the impact parameter (b) is the perpendicular distance between the momentum vectors of the two nuclei. For central collisions $b = 0$, for peripheral collisions $0 < b < 2R$, and for ultra-peripheral collisions $b \sim 2R$. These correspond to head-on, most central, and peripheral collisions, respectively. During the collisions, two areas of the nuclei that overlap are called an overlap region. The degree of overlapping is called centrality, which is related with the impact parameter. The centrality can be determined by measuring the number of nucleons that participate in the collision. The

nucleons in the overlap region are called participants, while the others are called spectators. The impact parameter, participant, and spectator are shown in Figure 3.1.

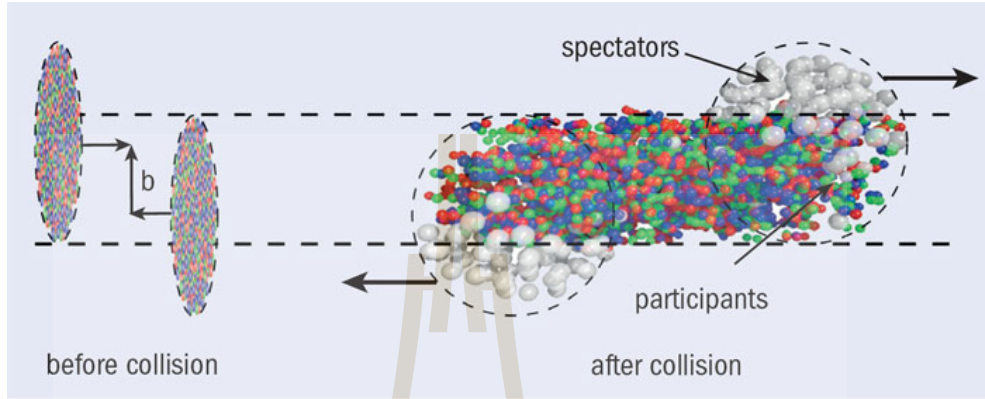


Figure 3.1 Left: Two nuclei before collision with impact parameter b . Right: participant and spectator nucleons during collision.

The centrality definition is not exclusive and can be defined by various quantities, such as impact parameter, the number of participants and the number of charged particles. Unfortunately, in heavy ion collision experiments, the impact parameter cannot be directly measured. Therefore, centrality is determined by particle multiplicity. In this work, we want to know how different centrality definition affect the cumulant ratios of net proton numbers. Therefore, the centrality will be defined by the number of charged particles (N_{charge}), number of participants (N_{part}) and number of participants in the projectile ($N_{\text{part-projectile}}$). We simulate Au+Au collisions at $\sqrt{s_{\text{NN}}}=7.7$ GeV with minimum bias collisions. We define the following quantities,

- N_{charge} : The number of all charged particles with $|\eta| \leq 1$ and $0.15 < p_{\text{T}} < 2.0$ GeV minus the number of protons and anti-protons in this specific acceptance range.
- N_{part} : 394 minus all spectator protons and neutrons with $|y| > 1.5$ and $p_{\text{T}} < 0.3$ GeV.
- $N_{\text{part-projectile}}$: 197 minus all projectile spectator protons and neutrons with $y > 1.5$ and $p_{\text{T}} < 0.3$ GeV.

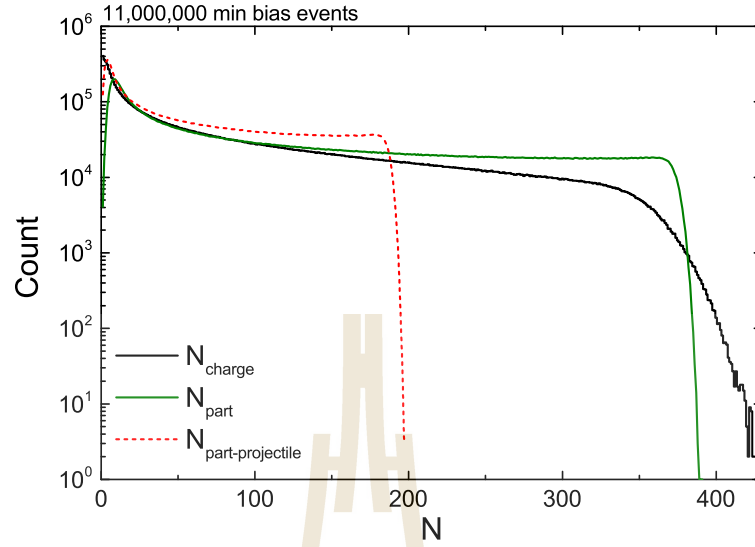


Figure 3.2 Distributions of N_{charge} , N_{part} and $N_{\text{part-projectile}}$ in minimum bias Au+Au collisions at $\sqrt{s_{\text{NN}}}=7.7$ GeV.

We should note that in our study, we define a spectator different from other transport model studies, where a spectator is strictly a nucleon that has not undergone any scattering. In experiments, such a definition is not measurable. Therefore, our definitions are motivated by the experimental definition of a spectator. However, we have also verified that our definition, which is based on the number of scatterings and our rapidity and p_{T} cut, gives similar results for the number of spectators. We used events around 11 million events which is generated with the UrQMD model. Figure 3.2 shows the distributions of N_{charge} , N_{part} and $N_{\text{part-projectile}}$. The three different centrality definition are different distributions. It is found that the participant distribution of N_{part} shows a sharp cutoff at the maximum number of participants, whereas the distributions of N_{charge} shows a much smoother drop. Next the centrality is classified into 10 centrality bins of 0-10%, 10-20%, 20-30%, 30-40%, 40-50%, 50-60%, 60-70%, 70-80%, 80-90% and 90-100%. Each centrality bin contains 10

Our first objective is to examine the correlation between the number of charged particles generated in a single event and the number of participants involved in that event. Figure 3.3 shows the distribution of N_{charge} as a function of N_{part} in an event. It is found that there is an apparent correlation,

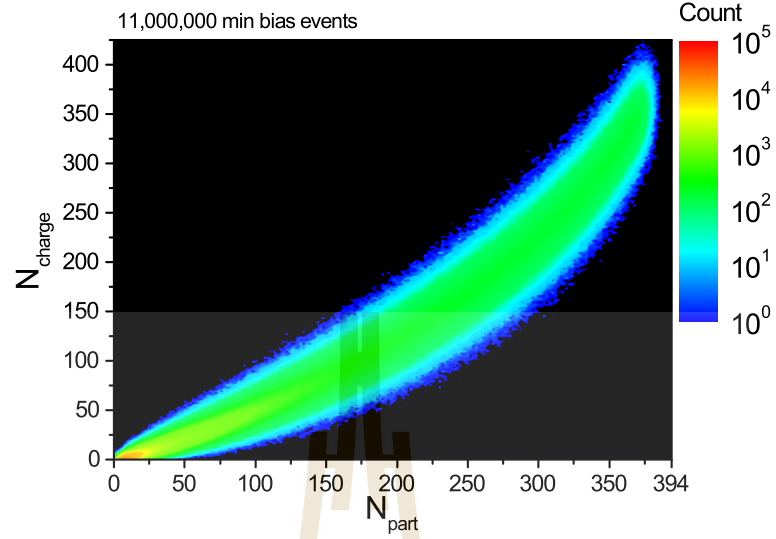


Figure 3.3 Distribution of N_{charge} as a function of N_{part} for 11 million minimum bias events.

however, the resulting distribution also shows a significant width in both N_{charge} and N_{part} .

Moreover, we calculate the correlation between N_{charge} and N_{part} or $N_{\text{part-projectile}}$ as a function of an impact parameter, as shown in Figure 3.4. The linear correlation coefficient (cor) can be defined as

$$\text{cor} = \frac{\sum_i (N_{\text{charge}}^i - \langle N_{\text{charge}} \rangle)(N_{\text{part}}^i - \langle N_{\text{part}} \rangle)}{\sigma_{\text{charge}} \sigma_{\text{part}}} . \quad (3.1)$$

where the sum always runs over all events in a given range of impact parameters b , with $\Delta b \equiv 3$ fm. The circle line denotes correlation between N_{part} and N_{charge} . The square line denotes correlation between $N_{\text{part-projectile}}$ and N_{charge} . The results shown that both the correlation for N_{part} and $N_{\text{part-projectile}}$ with N_{charge} shows a strength and centrality dependence. At very central and very peripheral collision show the weakest correlation between N_{part} , $N_{\text{part-projectile}}$ and N_{charge} whereas the strongest correlations are shown at the mid-central collision. Moreover, for the most central collisions, the number of participants is limited and the number of charged particles fluctuates significantly. For peripheral collisions, the number of participants only changes a little and is limited to $N_{\text{part}} > 1$, while the number of charged particles varies

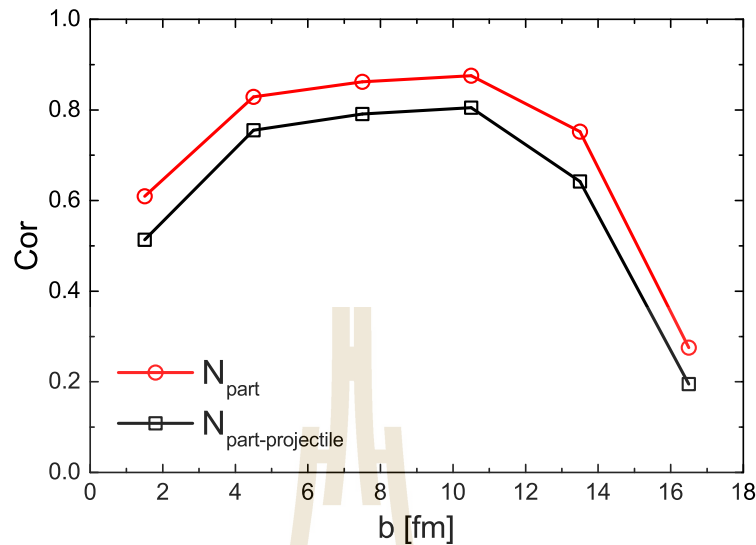


Figure 3.4 The correlation coefficient between N_{charge} and N_{part} or $N_{\text{part-projectile}}$ as a function of impact parameter in Au+Au collisions at $\sqrt{s_{\text{NN}}} = 7.7$ GeV. The circle line denotes correlation between N_{part} and N_{charge} . The square line denotes correlation between $N_{\text{part-projectile}}$ and N_{charge} .

more strongly.

3.2 Dependence on centrality definition

In this section, we will calculate the average of cumulants over a given centrality bin. There are 3 methods in principle as follows:

1. We calculate the cumulants C_n for a fixed N_{part} and then average the cumulants over all N_{part} in a given centrality bin. The cumulants ratios are taken as ratios of averages (Luo and Xu, 2017).
2. We calculate the cumulants ratios for a given N_{part} and then average the ratios over the centrality bin.
3. We calculate the variance, skewness, and kurtosis (σ , S and κ) for a given N_{part} and average them over a given centrality bin. Then appropriate average ratios are taken to get the ratios of cumulants.

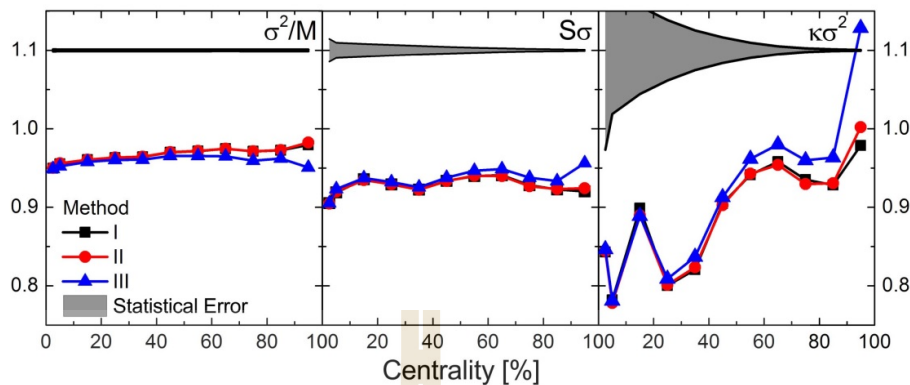


Figure 3.5 The ratios of cumulant of the net-proton number distributions as a function of centrality which is defined by N_{part} . It is shown in Figure 3.5. The square line denotes first method, the circle line denotes second method, the square line denotes third method and the grey band indicates the statistical error.

Note that all three methods should provide similar the results. The estimation of statistical errors is based on the delta-theorem, which is explained in Chapter II. Additionally, the equation of cumulants and cumulant ratios from chapter II is utilized.

The cumulant ratios of the net-proton number distributions as a function of centrality which is defined by N_{part} . It are shown in Figure 3.5. The square line denotes first method, the circle line denotes second method, the triangle line denotes third method and the grey band indicates the statistical error. It is found that the results of all three methods do agree well, but it is excepted for the most peripheral collisions. Because peripheral centrality bins the values of the cumulant ratios appear to be changing rapidly with centrality. Thus, the average of cumulant ratios depend on the method that is used to calculate them. Therefore, we will use first method for calculation the cumulant ratios in next section.

We assumed that the detection efficiency and acceptance are perfect (100%) for all particles used to determine the centrality. Figure 3.6 shows the results of $\kappa\sigma^2$ of the net-proton number as a function of centrality for the three centrality definition at mid-rapidity $|y| < 0.5$ and within transverse

momentum $0.4 < p_T < 0.8$ GeV. The square line denotes centrality as defined by N_{charge} , while the circle and triangle lines denote centrality as defined by N_{part} and $N_{\text{part-projectile}}$, respectively. We found that the value of $\kappa\sigma^2$ does not depend on the different centrality definitions, although the different definitions are only weakly correlated, as shown in Figure 3.4. This indicates that, although the measures of centrality are weakly correlated, the effective volume is essentially fixed and ‘volume fluctuations’ do not contribute strongly to the observed cumulant ratios. When we increase the centrality, the $\kappa\sigma^2$ gives the different value for all three centrality definition. In particular, the centrality is defined by $N_{\text{part-projectile}}$, which indicates that the value of $\kappa\sigma^2$ increases significantly for 40% – 60% of the most central collisions. It is clear that the number of target participants is allowed to fluctuate, leading to a significant increase in measured cumulant ratios. Moreover, the centrality defined by N_{charge} has a weak effect on the kurtosis. Because the charged particles are also measured around mid-rapidity, their multiplicity is more strongly correlated with the mid-rapidity ‘volume’ and therefore with the number of protons at mid-rapidity. Thus, we will use N_{charge} to define the centrality for investigating other effects.

3.3 Effects of transverse momentum (p_T) acceptance

In this section, we investigate the kurtosis of the net-proton number as a function of centrality which is defined by N_{charge} for two different p_T acceptances. The results of two different transverse momentum for the protons and anti-protons used to calculate the kurtosis is shown in Figure 3.7. The square line denotes $0.4 < p_T < 0.8$ GeV and the circle line denotes $0.4 < p_T < 2.0$ GeV. It is found that for the most central collisions, the value of the kurtosis is significantly reduced for the larger p_T acceptance due to the baryon number conservation. For mid-central collisions, the value of the kurtosis is larger in the case of increased p_T acceptance which indicates that volume fluctuations have effect on the kurtosis.

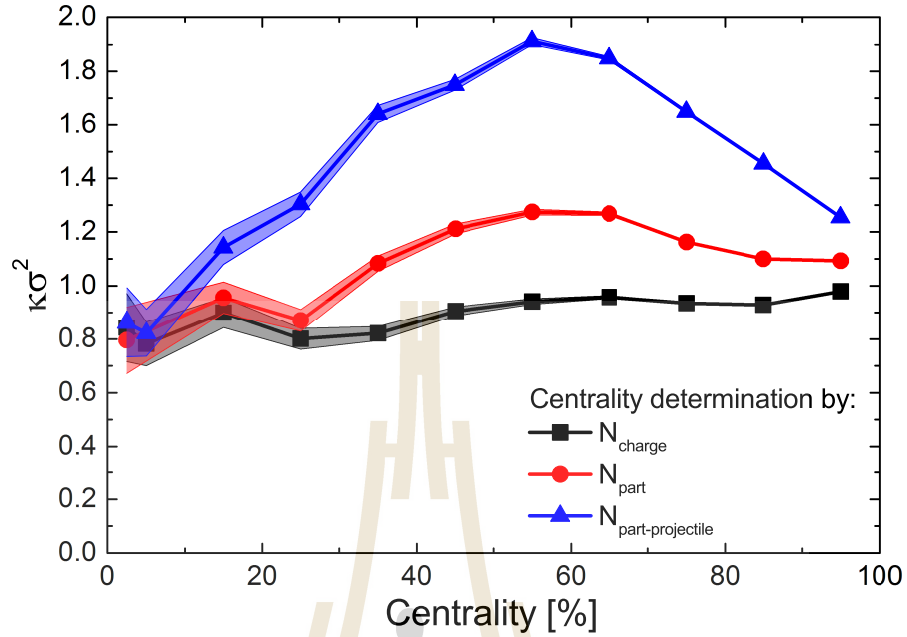


Figure 3.6 The results of $k\sigma^2$ of the net-proton number as a function of centrality for the three centrality definitions at mid-rapidity $|y| < 0.5$ and within transverse momentum $0.4 < p_T < 0.8$ GeV. The square line denotes centrality as defined by N_{charge} , while the circle and triangle lines denote centrality as defined by N_{part} and $N_{part-projectile}$, respectively.

3.4 Effects of efficiency

In experiments, particle detectors were not ideal systems and suffered from finite particle detection efficiency. This efficiency is defined as the number of particles that are produced and subsequently recorded in the detector, divided by the overall yield (Abelev et al., 2009). This means that the detector used to measure particle number distributions can never perform perfectly. Therefore, we will show how if the efficiency of the detector is less than 100% this will have an effect on the measurement of the cumulant ratios of the net proton number.

Firstly, we study the effects of efficiency on centrality definition. Figure 3.8 shows the results of the kurtosis of the net-proton number as a function of centrality which is defined by N_{charge} within two different p_T acceptance. The open and solid square lines denote the efficiency of N_{charge} at 100 and 70% within $0.4 < p_T < 0.8$ GeV, respectively. The open and solid circle lines

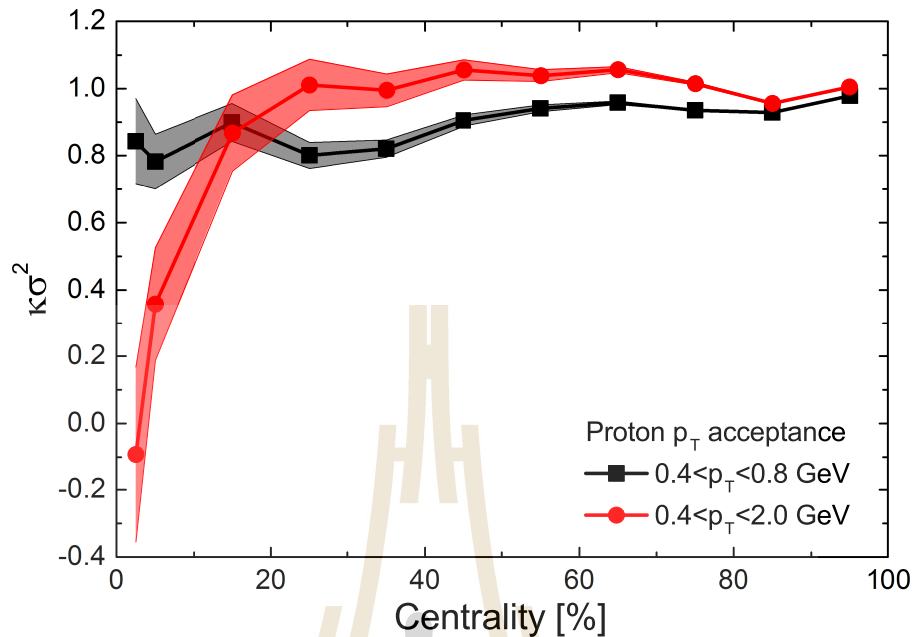


Figure 3.7 The kurtosis of the net-proton number as a function of centrality which is defined by N_{charge} for two different p_T acceptance. The square line denotes $0.4 < p_T < 0.8$ GeV and the circle line denotes $0.4 < p_T < 2.0$ GeV.

denote the efficiency of N_{charge} at 100 and 70% within $0.4 < p_T < 2.0$ GeV, respectively. It is found that the reduced efficiency leads to an increase in kurtosis.

Secondly, we study the effects of proton efficiency. The cumulant ratios of the net-proton number as a function of centrality which is defined by 70% efficiency N_{charge} within $0.4 < p_T < 2.0$ GeV is shown in Figure 3.9. The circle line denotes the proton efficiency at 100% (true), the square line denotes the proton efficiency at 75% (uncorrected). It is found that the results of the cumulant ratios of the net-proton number for the 75% proton efficiency are smaller than the 100% proton efficiency that is observed in the experimental data. For the most central events, the results of the cumulant ratios are decreased due to efficiency. It is the opposite behavior from what is observed in the analysis of the STAR experiment data because the results of STAR data for central collisions demonstrate the greatest efficiency corrections (Luo and Xu, 2017).

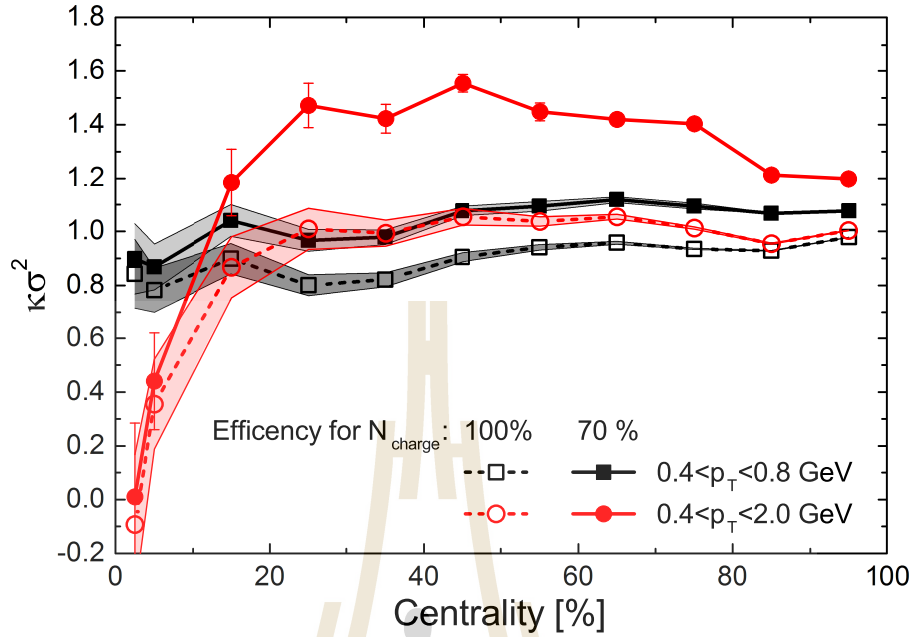


Figure 3.8 The kurtosis of the net-proton number as a function of centrality (defined by N_{charge}) within two different p_T acceptance.

3.5 Effects of rapidity dependence

In the following, we study the dependence of the cumulant ratios on the size of the rapidity acceptance Δy . In Figure 3.10 shows the dependence of the kurtosis and skewness of proton number on the size of the rapidity window, $0.0 \leq y \leq 2.0$, within $0.4 < p_T < 2.0$ GeV. The circle line denotes the results of kurtosis and the square line denotes the results of skewness. It is found that as the rapidity increases, the kurtosis and skewness tend to decrease. This phenomenon can be attributed to the increasing impact of baryon number conservation. This effect is particularly strong for kurtosis compared to skewness. For very small rapidity windows, the cumulants should resemble those of a Poisson distribution, i.e., they should converge towards 1, which is also observed.

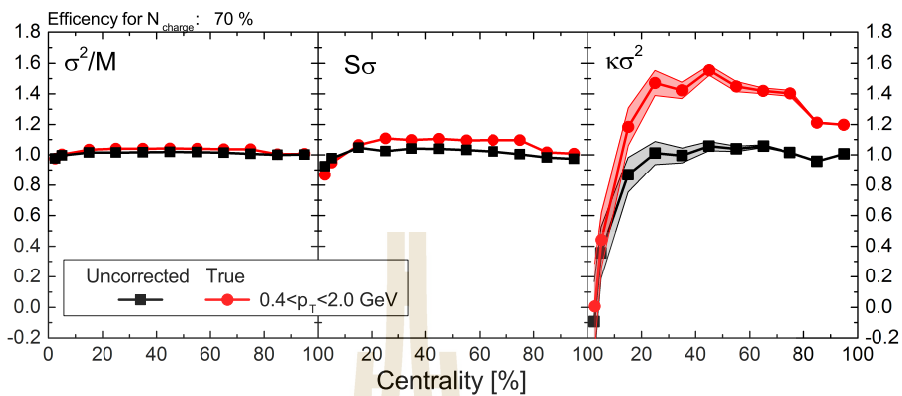


Figure 3.9 The result of cumulant ratios of net-proton number as a function of centrality which is defined by 70% N_{charge} efficiency within $0.4 < p_T < 2.0$ GeV. The circle line denotes the proton efficiency at 100% (true), the square line denotes the proton efficiency at 75% (uncorrected).

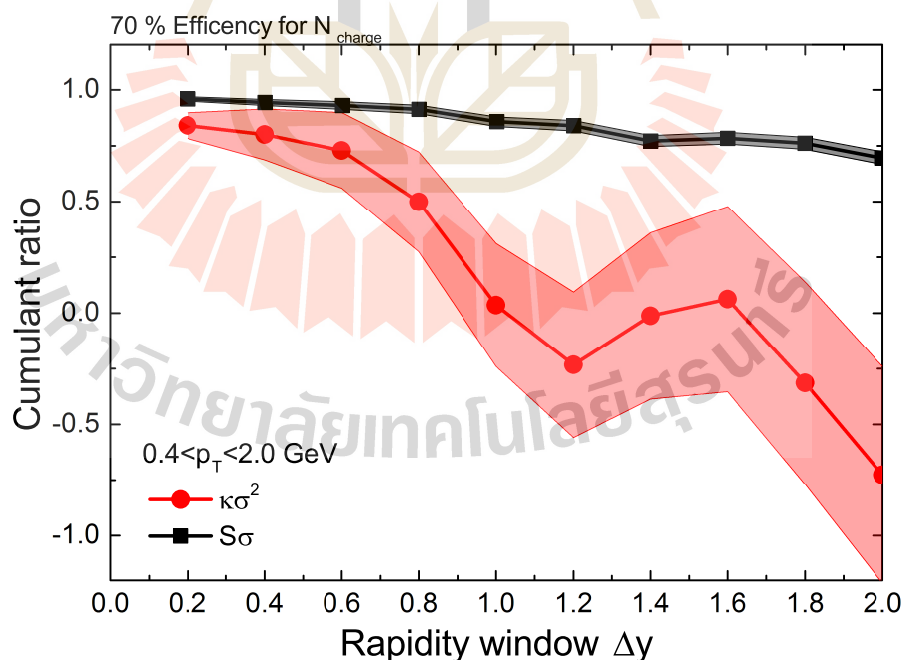


Figure 3.10 The dependence of the kurtosis and skewness of proton number on the size of the rapidity window, $0.0 \leq y \leq 2.0$, within $0.4 < p_T < 2.0$ GeV.

CHAPTER IV

DEUTERON PRODUCTION

The aim of the collision of heavy and light ions is to explore the dynamics and properties of strongly interacting matter which is governed by the laws of quantum chromodynamics (QCD). QCD matter under extreme conditions has been present since the first microseconds after the big bang and is also present in neutron star mergers and other compact stellar objects. An ideal environment for studying dense QCD matter in the laboratory is provided by the collision of light and heavy ions in accelerators such as the SIS18 at GSI or at the future Facility for Antiproton and Ion Research (FAIR) facility. These collisions can probe energies similar to those previously explored in experiments at the BNL Alternating Gradient Synchrotron (BNL-AGS) and the CERN Super Proton Synchrotron (CERN-SPS), particularly in the beam energy scan run by NA49 experiment. Nowadays systematic studies of dense QCD matter are ongoing through programs at the CERN-SPS (NA61 experiment) and the Relativistic Heavy Ion Collider Beam Energy Scan (RHIC-BES) (STAR experiment). The production of nuclear clusters, such as deuterons, is particularly interesting because it can shed light on the formation process, e.g., direct thermal production or coalescence. The thermal model supposes that the deuteron comes to equilibrium with hadrons until its individual points of chemical freeze-out. The deuteron is formed inside of fireball. The yields of deuteron have been accurately characterized by the results of thermal models (Shuryak and Torres-Rincon, 2020; Andronic et al., 2021; Wang et al., 2020). In contrast, the coalescence model assumes that the deuteron is produced by the coalescence of nucleons outside of the fireball's phase space. In this work, we study the deuteron production that is performed in UrQMD via phase space coalescence at the point of last interaction of the proton and neutron in space and time. We will present calculations of yields, ratios, and rapidity distributions of deuteron compared to experimental data.

The old version of UrQMD does not include the formation of deuterons or other nuclear clusters. To calculate the abundances and spectra of nuclear clusters are possible at different approaches. For instance, the cluster production in the UrQMD hybrid approach (Steinheimer et al., 2012) was calculated via

the Cooper-Frye equation on a hypersurface of constant energy density. This approach assumes that the deuterons are not formed by coalescence but they are emitted as a single entity from the fireball as suggested in statistical hadronization models. An alternative way is the coalescence approach introduced by the Gyulassy, Frankel, and Remler approach (Gyulassy et al., 1983) based on the von Neumann equation for the n-body density $\rho(t)$. The cross section to observe a deuteron in the final state is then given by

$$\sigma_D = \lim_{t \rightarrow \infty} \text{Tr} \rho_D \rho(t) \quad (4.1)$$

with ρ_D being the Wigner transform of the deuteron state. This Wigner function approach follows the original idea of Sato and Yazaki (Sato and Yazaki, 1981). The formation of deuterons in Wigner function approach is calculated at the last point of interaction of either nucleon. The Wigner function approach has been applied very successfully in the description of deuteron production. It is shown in (Aichelin and Remler, 1987; Nagle et al., 1994; Ko et al., 2010; Zhu et al., 2015)

Finally, it is possible to use a direct coalescence approach, either in momentum space or coordinate space or in full phase space. One defines a maximum relative momentum Δp and/or a maximum distance Δr between the proton and the neutron to form a deuteron. This approach is similar to the Wigner function approach but essentially assumes a flat probability in coordinate space and momentum space for the coalescence probability (instead of the deuteron wave function). Phase-space coalescence has been shown to work successfully and to yield results similar to the Wigner function approach (Nagle et al., 1994). Therefore, in this work, we model deuteron production in UrQMD via phase space coalescence at the point of last interaction of the respective proton and neutron in space and time. The method we will use is the following:

1. We follow the protons and neutrons through the evolution of the system until their individual space-time points of last interaction.
2. For each p-n pair the momentum and position of proton and neutron is boosted to the 2-particle restframe of this p-n pair.
3. The particle that dissociated earlier is then propagated to the other particle

later time.

4. We calculate the relative momenta $\Delta p = |\vec{p}_1 - \vec{p}_2|$ and the relative distances $\Delta r = |\vec{x}_1 - \vec{x}_2|$ of the p-n pair in the 2-particle restframe at equal times. The yield of deuteron candidates is given by the condition of $\Delta p < \Delta p_{\max}$ and $\Delta r < \Delta r_{\max}$. Here we use the set of parameter $\Delta p_{\max} = 0.285$ GeV/c and $\Delta r_{\max} = 3.575$ fm.

5. We operate the statistical spin and isospin projection to the deuteron state (probability $1/2 \times 3/4 = 3/8$) (Aichelin and Remler, 1987) for each deuteron candidate. Then, the chosen p-n pair is recorded as a deuteron and cannot be used to produce another deuteron.

Note that the parameters for deuteron formation are independent of energy, the collision system, and centrality. We will find that the parameter values are chosen to give a good description of the available data for a wide range of systems and beam energies.

4.1 Proton-induced reaction

Proton induced reactions are the simplest to study in our model studies. In these systems, the rescattering stage is rather short and the freeze-out volumes are smaller than in nucleus-nucleus reactions.

The rapidity distributions of protons and deuterons in minimum bias p+Au (left) and p+Be (right) collisions at a beam energy of 14.6A GeV are calculated. It is shown in Figure 4.1. The lines indicate the UrQMD calculations and the circle symbol denotes the E802 experimental data (Abbott et al., 1993). y is the rapidity which can be seen in appendix B for more detail. It is found that the deuteron and proton yields are consistent with the E802 experimental data and the rapidity distributions are well reproduced. The distributions of protons and deuterons are found a lot at $y = 0$. Because the ejection of protons and deuterons occur mainly in the target fragmentation region. The protons shows an approximate symmetry around the center-of-mass rapidity ($y_{c.m} = y_{beam}/2 = 1.72$). It indicates that these collisions are dominated by single nucleon-nucleon collisions.

Moreover, the integrated yields (dN/dy) of deuterons and antideuterons in p + p collisions with midrapidity $|y| < 0.5$ are calculated by the UrQMD model at

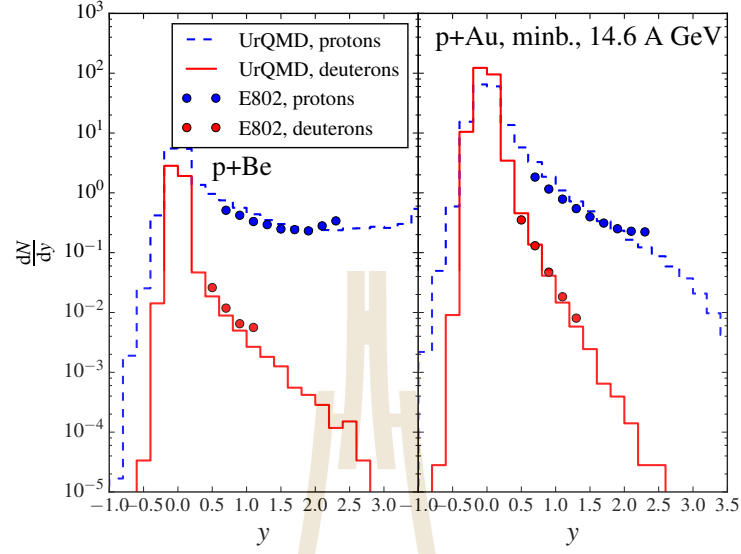


Figure 4.1 Rapidity distributions of protons and deuterons in minimum bias p+Be (left) and p+Au (right) collisions at a beam energy of 14.6A GeV. The lines indicate the UrQMD calculations and the solid circle denotes the E802 experimental data (Abbott et al., 1993).

different center-of-mass energies $\sqrt{s_{NN}} = 0.9, 2.76, \text{ and } 7 \text{ TeV}$ and compared to ALICE experimental data, as shown in Table 4.1. We can see that our results are in agreement with the ALICE experimental data.

Table 4.1 The integrated yield (dN/dy) of deuterons and anti-deuterons in p+p collisions with midrapidity $|y| < 0.5$ at different center of mass energies as $\sqrt{s_{NN}} = 0.9, 2.76 \text{ and } 7 \text{ TeV}$.

		dN/dy	
$\sqrt{s_{NN}}$ (TeV)		ALICE	UrQMD
d	0.9	$(1.12 \pm 0.09 \pm 0.09) \times 10^{-4}$	$(0.96 \pm 0.05) \times 10^{-4}$
	2.76	$(1.53 \pm 0.05 \pm 0.13) \times 10^{-4}$	$(1.47 \pm 0.06) \times 10^{-4}$
	7	$(2.02 \pm 0.02 \pm 0.17) \times 10^{-4}$	$(2.05 \pm 0.09) \times 10^{-4}$
\bar{d}	0.9	$(1.11 \pm 0.10 \pm 0.09) \times 10^{-4}$	$(1.00 \pm 0.05) \times 10^{-4}$
	2.76	$(1.37 \pm 0.04 \pm 0.12) \times 10^{-4}$	$(1.55 \pm 0.07) \times 10^{-4}$
	7	$(1.92 \pm 0.02 \pm 0.15) \times 10^{-4}$	$(2.22 \pm 0.09) \times 10^{-4}$

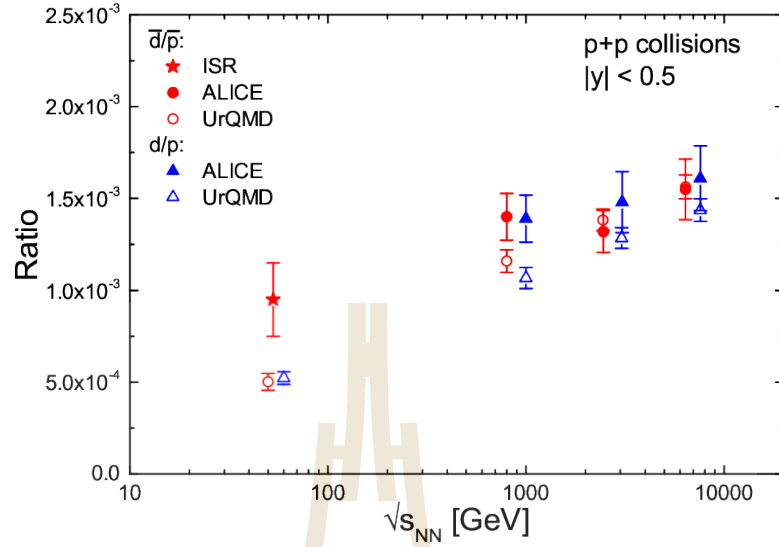


Figure 4.2 Energy dependence of d/p and \bar{d}/\bar{p} ratios in pp collisions with $|y| < 0.5$ at $\sqrt{s_{NN}} = 53, 900, 2760$ and 7000 GeV. The open circle and triangle are calculated by the UrQMD model, the solid star denotes the results from ISR (Alper et al., 1973; Henning et al., 1978; Alper et al., 1975) and the solid circle and triangle denote the results from ALICE experimental data.

From the integrated yields in Table 4.1, one can calculate the ratios of deuteron to proton (d/p) and antideuteron to antiproton (\bar{d}/\bar{p}) as a function of energies $\sqrt{s_{NN}} = 53, 900, 2760$ and 7000 GeV, as shown in Figure 4.2. The open circle and triangle are calculated by the UrQMD model and compared to the experimental data. The solid star denotes the results from ISR (Alper et al., 1973; Henning et al., 1978; Alper et al., 1975) and the solid circle and triangle denote the results from ALICE experimental data (Acharya et al., 2018). It is found that, at high energies, our results are consistent with the ALICE experimental data. The results of this ratio increase with increasing energies.

4.2 Nucleus-nucleus reaction

Next, we will present the results of deuteron and antideuteron production for collisions of light to heavy nuclei at various beam energies. At lowest beam energies, we compare the rapidity distributions ($dN/dy^{(0)}$) of deuterons, protons, and π^- in Ni+Ni collisions with $b \leq 1.8$ fm at beam energies of 1.93A, 1.45A and 1.06A GeV within UrQMD model. Our results are compared

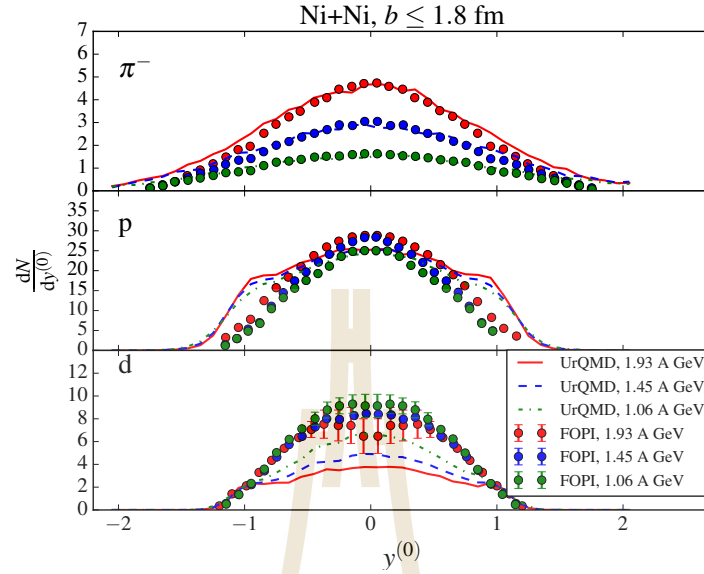


Figure 4.3 The $dN/dy^{(0)}$ distributions of deuterons, protons and π^- for Ni+Ni collisions with $b \leq 1.8$ at beam energies of 1.93A, 1.45A and 1.06A GeV. The lines indicate the UrQMD model and the circle symbols denote the FOPI experiment (Hong et al., 1998).

to the data from the FOPI experiment, as shown in Figure 4.3. The lines indicate the UrQMD model and the circle symbols denote the FOPI experimental data (Hong et al., 1998). Here the normalized rapidity $y^{(0)} = y/y_{cm}$ is the rapidity scaled with the center-of-mass rapidity y_{cm} . We found that our results are consistent with the FOPI data. For these low beam energies, the deuteron yields are observed as deviations at forward and backward rapidities. However, these deviations are expected for the lowest beam energies because we did not include the effects of nuclear potential interactions in our simulations. Moreover, the results show that the rapidity distributions of protons and deuterons have a similar shape at different energies. However, the magnitude of the rapidity distributions of the protons is increased, whereas the magnitude of the deuteron rapidity distributions decreases with increasing beam energy. For higher beam energies, the results of our calculations in Au+Au collision at a beam energy 10.8A GeV are presented in Figures 4.4 and 4.5, respectively. Figure 4.4 shows the rapidity distributions (dN/dy) of protons and deuterons (time 5) in Au+Au collisions at a beam energy 10.8A GeV with $b = 3$ fm. The dashed lines indicate our simulations and the circle symbol denotes the E917 experimental

data (Back et al., 2001). It is found that the rapidity distributions of protons and deuterons are peaked around midrapidity (in the laboratory frame), due to the increased stopping power in the symmetric heavy-ion collision. Moreover, Figure 4.5 shows invariant yields of deuterons at $p_t = 0$ as a function of rapidity in central collisions which are shown on the left hand side and minimum-bias which are shown on the right hand side, in Au+Au collisions at a beam energy of 10.8A GeV. The lines show the UrQMD model calculations which are compared to the E878 experiment data (Bennett et al., 1998) which is the circle symbol.

The expression for the invariant yield of deuterons as a function of velocity is

$$E \frac{d^3N}{dp^3} = \frac{1}{2\pi p_t} \frac{d^2N}{dp_t dy}, \quad (4.2)$$

where E is the energy and p_T is the transverse momentum

$$p_t = \sqrt{p_x^2 + p_y^2}, \quad (4.3)$$

where p_x and p_x are the momentum components in the transverse momentum plane. It is found that our calculations are consistent with the E878 experimental data. The yields in central collisions are higher than in minimum-bias collisions due to the increased stopping in central collisions.

In the following, we present results of deuteron production in various colliding systems at a beam energy of 14.6A GeV. A wealth of deuteron measurements were taken, which allow a systematic comparison with our model calculations. At this beam energy, the deuteron measurements allow a systematic comparison with our model calculations. Figure 4.6 shows the rapidity distributions of protons and deuterons in Si+Au collisions at a beam energy of 14.6A GeV with $b=2$ fm. The lines indicate our model calculations and the circle symbols denote the E802 experimental data (Abbott et al., 1994). From the results, we observed that the rapidity distributions of protons and deuterons are in reasonable agreement with E802 experimental data. Figure 4.7 shows invariant yields of deuterons as a function of rapidity in central which is shown on the left hand side and minimum-bias which is shown on the right hand side in Si+Pb collisions at a beam energy of 14.6A GeV at $p_t = 0$. The lines indicate the UrQMD calculations and the circle symbols denote the E814 experimental data (Anticic et al., 2016). It is found that the invariant yields measured in

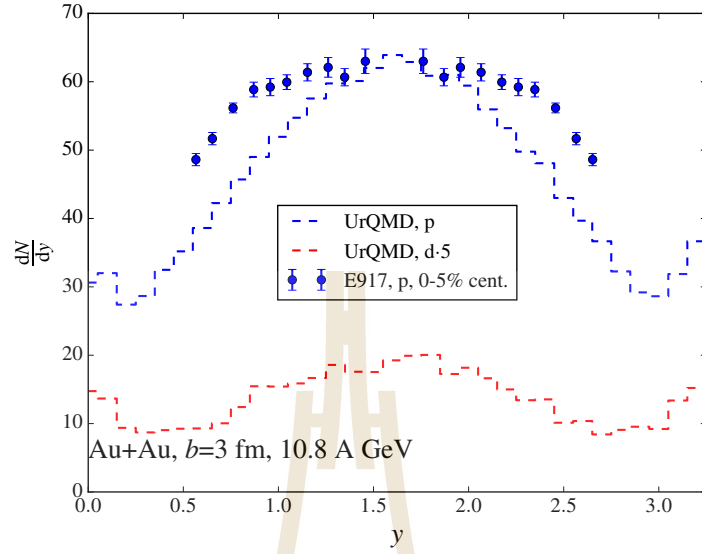


Figure 4.4 Rapidity distributions of protons and deuterons (times 5) in Au+Au collisions at a beam energy of 10.8A GeV with $b = 3$ fm. The dashed line indicates our simulation and the circle symbol denotes the E917 experimental data (Back et al., 2001).

our simulation are consistent with the E814 experimental data. The yields of deuterons in central collisions are higher than in minimum-bias collisions due to the increased stopping in central collisions.

Moreover, the invariant yields of deuterons as a function of $m_t - m$ in central Si+Al, Si+Cu and Si+Au collisions at a beam energy 14.6A GeV are calculated by UrQMD model and compared to the experiment E802 data (Abbott et al., 1994), as shown in Figure 4.8. The lines indicate the UrQMD calculations and the circle symbols denote the E802 experimental data. The central collisions ,the rapidity interval is $y = 0.5$ to 1.5 with $\Delta y = 0.2$. Each successive spectrum is divided by 100 for visual clarity. The invariant yields is defined as

$$E \left(\frac{d^3N}{dp^3} \right) = \frac{1}{2\pi m_t} \frac{d^2N}{dy dm_t}, \quad (4.4)$$

where m_t is the transverse mass

$$m_t = (p_t^2 + m^2)^{1/2}, \quad (4.5)$$

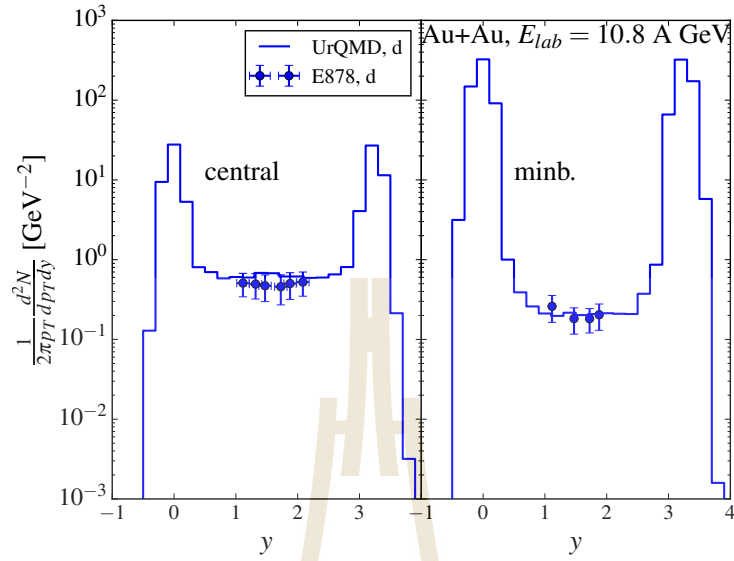


Figure 4.5 Invariant yields of deuterons at $p_t = 0$ as a function of rapidity in central (left) and minimum-bias (right) Au+Au collisions at a beam energy of 10.8A GeV. The lines denote the UrQMD model calculations, the circle symbol denotes the E878 experiment data (Bennett et al., 1998).

It is found that our results are consistent with the E802 experimental data. The resulting invariant yields of deuterons for the three targets for each rapidity interval show that the invariant yields are decreased with increasing rapidity value until the fragmentation region.

In the next step, we explore deuteron formation at various energies and centralities. Figure 4.9 shows the deuteron distributions as a function of rapidity in Pb+Pb collisions at a beam energy of 20A GeV for different centralities. The lines denote the UrQMD calculations and the circle symbols denote the NA49 experimental data (Anticic et al., 2016). It is found that our results are in good agreement with the NA49 experimental data. However, we can observe a small deviation in the experimental data that the baryon stopping in UrQMD is stronger than the NA49 data, when going towards more central collisions. Moreover, Figure 4.10 shows the deuteron distributions as a function of rapidity at beam energies 20A GeV, 30A GeV, 40A GeV, 80A GeV, and 158A GeV in central Pb+Pb collisions. The lines denote the UrQMD calculations and the circle symbols denote the experimental data of the NA49 collaboration (Anticic et al., 2016). For visibility the calculations and the data are successively divided by a

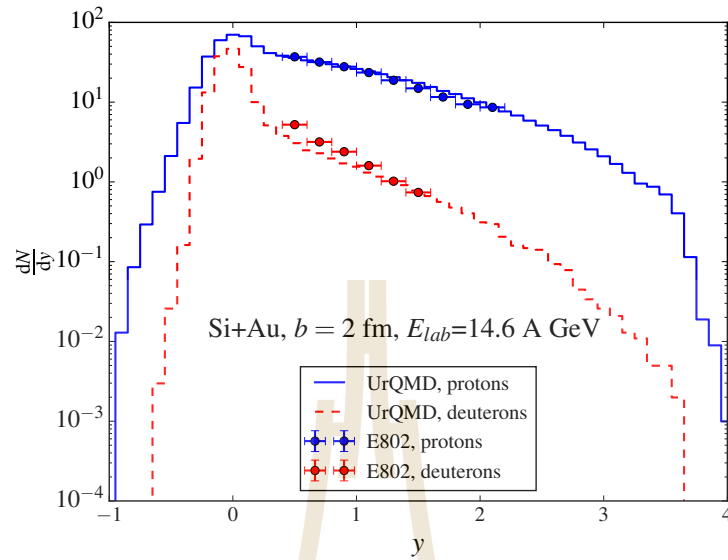


Figure 4.6 Rapidity distributions of protons and deuterons in Si+Au collisions at a beam energy of $14.6A$ GeV with impact parameter $b = 2$ fm. The lines indicate our model calculations and the circle symbols denote the E802 experimental data (Abbott et al., 1994).

factor of 10. It is found that are consistent with the NA49 experimental data. From the results represented above, it has been demonstrated that deuteron production at medium energies can be very well described by a phase-space coalescence parameter set.

Finally, we show the invariant yields of anti-deuterons (\bar{d}) and anti-protons (\bar{p}) at $p_t = 0$ as a function of rapidity in Si+Au collisions at a beam energy of $14.6A$ GeV with $b = 2$ fm. Our results are compared to the data from the E858 (Shiva et al., 1994) and E814 (Barrette et al., 1993) experiments, it is shown in Figure 4.11. The lines denote the UrQMD calculation. The circle symbols denote the E858 and E814 experimental data. It is found that our results are consistent with the experimental data.

4.3 Excitation function

In this section, the ratio of the deuteron to proton and antideuteron to antiproton as a function of energy dependence in Au+Au collisions with $b \leq 4.6$ fm and mid-rapidity ($|y| < 0.3$) are calculated. It is shown in Figure 4.12. The

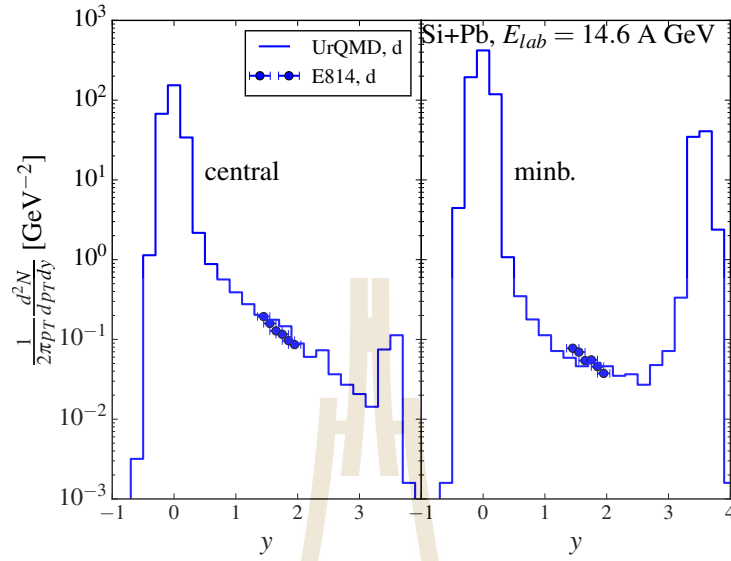


Figure 4.7 Invariant yields of deuterons at $p_t = 0$ as a function of rapidity in central (left) and minimum-bias (right) Si+Pb collisions at a beam energy of 14.6A GeV. The lines indicate the UrQMD calculations and the circle symbols denote the E814 experimental data (Anticic et al., 2016)

UrQMD calculations are compared to a thermal model fit (Andronic et al., 2011) and experimental data from the SIS (Cleymans et al., 1999), E802 (Ahle et al., 1999), PHENIX (Adler et al., 2005), NA49 (Anticic et al., 2016), STAR (Yu, 2017), ALICE (Anielski, 2015), and E814 collaboration (Barrette et al., 1993). The solid lines denote UrQMD calculation, the dotted line denote thermal model fit and the symbols denote the experimental data from various collaborations. It is found that our results are consistent with both the thermal model and the experimental data. The ratio of d/p decreases with increasing higher energies due to the decreasing phase space density for baryons at higher beam energies. The ratio of \bar{d}/\bar{p} decreases with decreasing lower energies which indicates the surface freeze-out of the anti-protons and thus also a decreased phase space density (Mrowczynski, 1993; Bleicher et al., 1995).

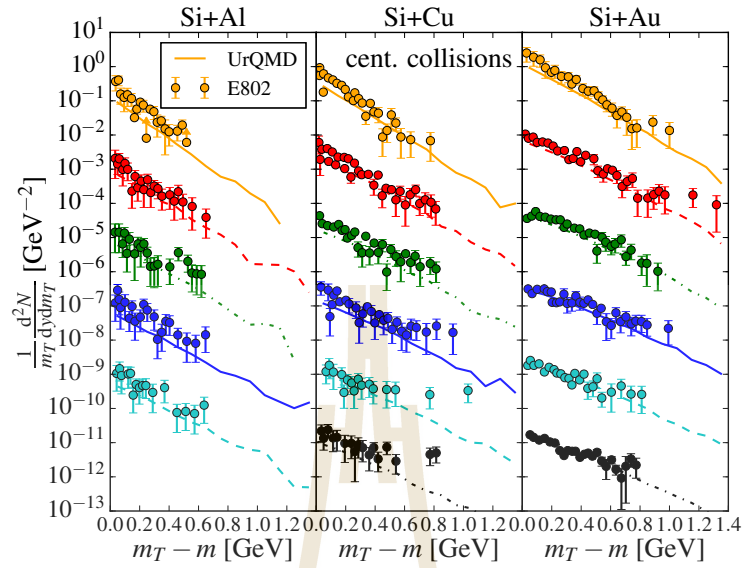


Figure 4.8 Invariant yields of deuterons as a function of $m_t - m$ in central Si+Al, Si+Cu and Si+Au collisions at a beam energy of $14.6A$ GeV. The rapidity interval is $y = 0.5$ to 1.5 with $\Delta y = 0.2$. Each successive spectrum is divided by 100 for visual clarity. The circle symbols denote the E802 experimental data (Abbott et al., 1994) and the lines indicate the UrQMD calculations.

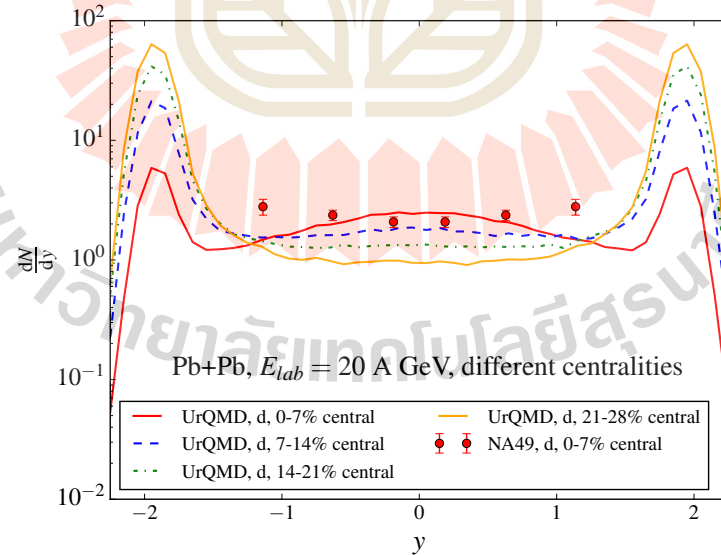


Figure 4.9 Deuteron distributions as a function of rapidity in Pb+Pb collisions at a beam energy of $20A$ GeV for different centralities. The lines denote the UrQMD calculations and the circle symbols denote the NA49 experimental data (Anticic et al., 2016) and the lines denote the UrQMD calculations.

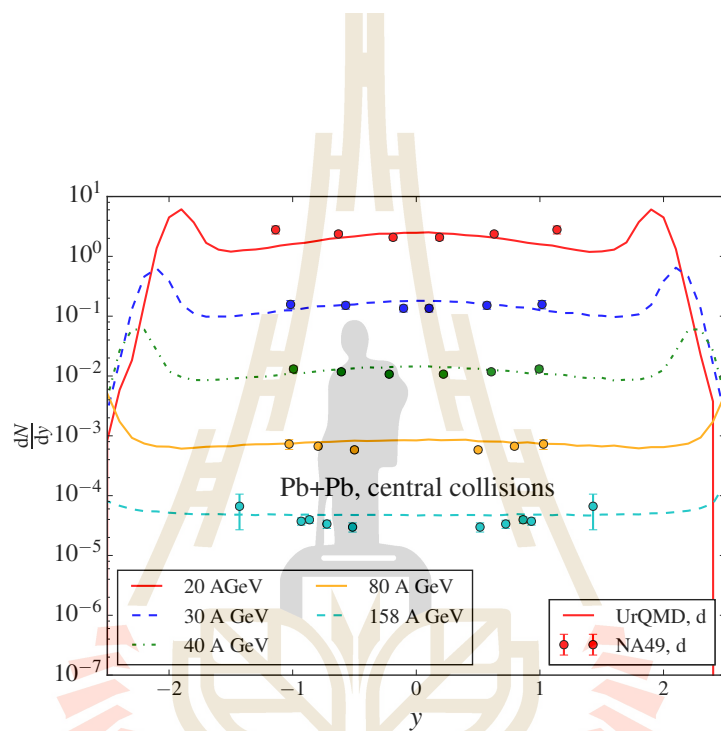


Figure 4.10 Deuteron distributions as a function of rapidity at beam energies 20A GeV, 30A GeV, 40A GeV, 80A GeV, and 158A GeV in central Pb+Pb collisions. The circle symbols denote the NA49 experimental data (Anticic et al., 2016) and the lines show the UrQMD calculations. Each spectrum are successively divided by a factor of 10.

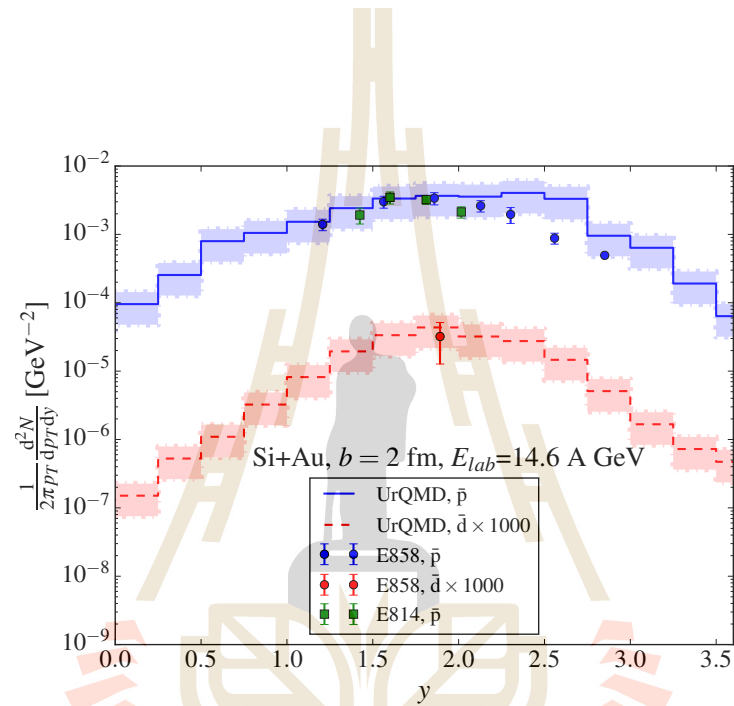


Figure 4.11 The invariant yields of anti-deuterons (\bar{d}) and anti-protons (\bar{p}) at $p_t = 0$ as a function of rapidity in Si+Au collisions at a beam energy of 14.6A GeV with $b = 2$ fm. Our results are compared to the data from the E858 (Shiva et al., 1994) and E814 (Barrette et al., 1993) experiments. The lines denote the UrQMD calculation. The circle symbols denote the E858 and E814 experimental data.

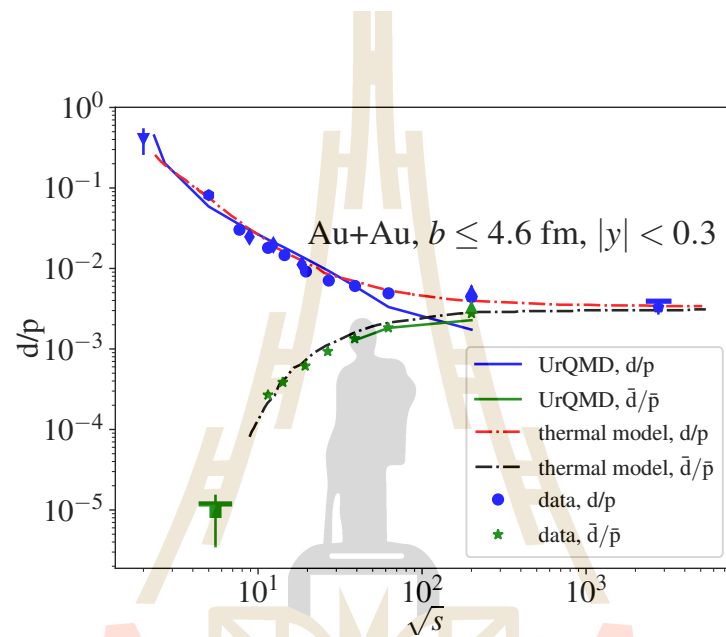


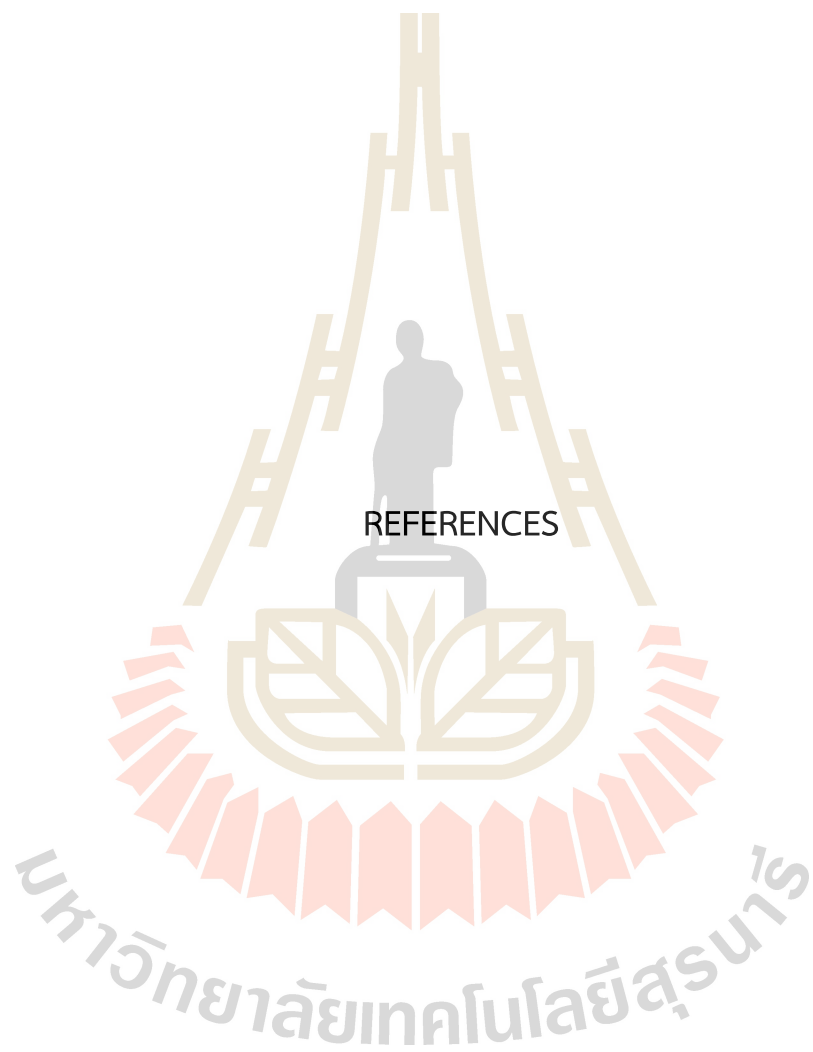
Figure 4.12 The ratio of deuteron to proton ratio and a function of energy dependence in Au+Au collisions with $b \leq 4.6$ fm and $|y| < 0.3$. The solid lines denote UrQMD model results, the dotted lines denote the thermal model fit (Andronic et al., 2011) and symbols denote experimental data from various collaborations (triangle down: SIS (Cleymans et al., 1999), hexagon: E802 (Ahle et al., 1999), triangles up: PHENIX (Adler et al., 2005), diamonds: NA49 (Anticic et al., 2016), circles: STAR (Yu, 2017), pentagon: ALICE (Anielski, 2015), square: E814 (Barrette et al., 1993)).

CHAPTER V

CONCLUSIONS

In this work, we study the effect of different methods for centrality definition on the measured net-proton kurtosis. Three centrality definitions (N_{charge} , N_{part} , $N_{\text{part-projectile}}$) give different results of kurtosis. N_{charge} is used for the centrality definition because it has the smallest dependence of the cumulant ratios. Moreover, we have studied the effects of p_T acceptance and rapidity windows. We have demonstrated that for the most central collisions, the value of the kurtosis is significantly reduced for the larger p_T acceptance. An increasing rapidity window will give decreasing cumulant ratios. Finally, we explore the effects of centrality definition efficiency which is defined by N_{charge} and proton efficiency. We found that a smaller efficiency for N_{charge} leads to an increase in the kurtosis. Smaller efficiency for proton leads to the decrease of the kurtosis.

we investigate the deuteron production in the FAIR up to LHC energy regime using UrQMD + coalescence model. The UrQMD + phase space coalescence model with parameters $\Delta p_{\text{max}} = 0.285$ GeV/c and $\Delta r_{\text{max}} = 3.575$ fm provides a very good description of the available data of deuteron production. From the results for proton induced reactions (p+p and p+Au, p+Be) at low and high energies, forward Pb+Pb collision at the CERN-SPS and CERN-LHC is found that deuteron production for all systems can be described by coalescence with the same phase space parameters. Given the current discussion of the deuteron production at LHC, we want to stress that coalescence provides similar results for the d/p ratios as the thermal model over the whole range of expected energies. In addition it captures the decrease of the d/p ratio for the high centrality bin in Pb+Pb reactions at the LHC. Furthermore, our results of the distribution of deuterons and protons as a function of rapidity in Ni+Ni and Au+Au collision are consistent with the experiment data. Moreover, the result of the invariant yield of antideuterons and antiprotons at $p_t = 0$ as a function of rapidity in minimum-bias Si+Au collisions at 14.6A GeV found that the UrQMD calculation is in agreement with the E814 experimental data.



REFERENCES

REFERENCES

- Abbott, T., Akiba, Y., Beavis, D., Bloomer, M., Bond, P., Chasman, C., Chen, Z., Chu, Y., Cole, B., Costales, J., Crawford, H., Cumming, J., Debbe, R., Engelage, J., and Fung, S. et al. (1993). Measurement of particle production in proton-induced reactions at 14.6 GeV/c. *Physical Review D* 45, 3906–3920.
- Abbott, T., Akiba, Y., Beavis, D., Bloomer, M. A., Bond, P. D., Chasman, C., Chen, Z., Chu, Y. Y., Cole, B. A., Costales, J. B., Crawford, H. J., Cumming, J. B., Debbe, R., Engelage, J., and Fung, S.-Y. et al. (1994). Charged hadron distributions in central and peripheral Si+A collisions at 14.6A GeV/c. *Physical Review C* 50(2), 1024–1047.
- Abdallah, M. S., Adam, J., Adamczyk, L., Adams, J. R., Adkins, J. K., Agakishiev, G., Aggarwal, I., Aggarwal, M. M., Ahammed, Z., Alekseev, I., Anderson, D. M., Aparin, A., Aschenauer, E. C., Ashraf, M. U., and Atetalla, F. G. et al. (2021). Cumulants and correlation functions of net-proton, proton, and antiproton multiplicity distributions in Au + Au collisions at energies available at the BNL Relativistic Heavy Ion Collider. *Physical Review C* 104, 024902.
- Abelev, B. I., Aggarwal, M. M., Ahammed, Z., Anderson, B. D., Arkhipkin, D., Averichev, G. S., Bai, Y., Balewski, J., Barannikova, O., Barnby, L. S., Baudot, J., Baumgart, S., Beavis, D. R., Bellwied, R., and Benedosso, F. et al. (2009). Systematic measurements of identified particle spectra in pp , $d + Au$, and $Au + Au$ collisions at the STAR detector. *Physical Review C* 79, 034909.
- Acharya, S., Adam, J., Adamová, D., Adolfsson, J., Aggarwal, M. M., Aglieri Rinella, G., Agnello, M., Agrawal, N., Ahammed, Z., Ahmad, N., Ahn, S. U., Aiola, S., Akindinov, A., Al-Turany, M., and Alam, S. N. et al. (2018). Production of deuterons, tritons, ^3He nuclei, and their antinuclei in pp collisions at $\sqrt{s} = 0.9, 2.76, \text{ and } 7 \text{ TeV}$. *Physical Review C* 97, 024615.

- Adamczyk, L., Adkins, J. K., Agakishiev, G., Aggarwal, M. M., Ahammed, Z., Alekseev, I., Alford, J., Anson, C. D., Aparin, A., Arkhipkin, D., Aschenauer, E. C., Averichev, G. S., Banerjee, A., Beavis, D. R., and Bellwied, R. et al. (2014). Beam-Energy Dependence of the Directed Flow of Protons, Antiprotons, and Pions in Au+Au Collisions. *Physical Review Letters* 112, 162301.
- Adler, S. S., Afanasiev, S., Aidala, C., Ajitanand, N. N., Akiba, Y., Alexander, J., Amirkas, R., Aphecetche, L., Aronson, S. H., Auerbeck, R., Awes, T. C., Azmoun, R., Babintsev, V., Baldisseri, A., and Barish, K. N. et al. (2005). Deuteron and Antideuteron Production in Au + Au Collisions at $\sqrt{s_{NN}} = 200$ GeV. *Physical Review Letters* 94, 122302.
- Aggarwal, M. M., Ahammed, Z., Alakhverdyants, A. V., Alekseev, I., Anderson, B. D., Arkhipkin, D., Averichev, G. S., Balewski, J., Barnby, L. S., Baumgart, S., Beavis, D. R., Bellwied, R., Betancourt, M. J., Betts, R. R., and Bhasin, A. (2010). An Experimental Exploration of the QCD Phase Diagram: The Search for the Critical Point and the Onset of De-confinement. *arXiv e-prints*, 1007.2613.
- Ahle, L., Akiba, Y., Ashktorab, K., Baker, M. D., Beavis, D., Britt, H. C., Chang, J., Chasman, C., Chen, Z., Chi, C.-Y., Chu, Y. Y., Cianciolo, V., Cole, B. A., Crawford, H. J., and Cumming, J. B. et al. (1999). Proton and deuteron production in Au+Au reactions at 11.6A GeV/c. *Physical Review C* 60, 064901.
- Aichelin, J. and Remler, E. A. (1987). Deuteron and Entropy Production in Relativistic Heavy Ion Collisions. *Physics Review C* 35, 1291-1296.
- Alper, B., Boggild, H., Booth, P., Bulos, F., Caroll, L., Damgaard, G., Von Dardel, G., Duff, B., Hansen, K., Heymann, F., Jackson, J., Jarlskog, G., Jönsson, L., Klovning, A., and L. Leistam., et al. (1975). Production spectra of π^{\pm} , K^{\pm} , p^{\pm} at large angles in proton-proton collisions in the CERN intersecting storage rings. *Nuclear Physics B* 100(2), 237-290.
- Alper, B., Boggild, H., Booth, P., Bulos, F., Caroll, L., Damgaard, G., Von Dardel, G., Duff, B., Lillethun, E., Heymann, F., Jackson, J., Jarlskog, G., Jönsson,

- L., Klovning, A., and L. Leistam., et al. (1973). Large angle production of stable particles heavier than the proton and a search for quarks at the cern intersecting storage rings. *Nuclear Physics B* 46, 265–268.
- Alt, C., Anticic, T., Baatar, B., Barna, D., Bartke, J., Behler, M., Betev, L., Białkowska, H., Billmeier, A., Blume, C., Boimska, B., Borghini, N., Botje, M., Bracinik, J., and Bramm, R. et al. (2003). Directed and elliptic flow of charged pions and protons in Pb+Pb collisions at 40A and 158A GeV. *Physics Review C* 68, 034903.
- Andersson, B., Gustafson, G., and Soderberg, B. (1983). A General Model for Jet Fragmentation. *Zeitschrift für Physik C* 20, 317.
- Andronic, A., Barret, V., Basrak, Z., Bastid, N., Benabderrahmane, L., Berek, G., Čaplar, R., Cordier, E., Crochet, P., Dupieux, P., Dželalija, M., Fodor, Z., Gasparic, I., Grishkin, Y., and Hartmann, O. (2005). Excitation function of elliptic flow in Au+Au collisions and the nuclear matter equation of state. *Physics Letters B* 612, 173–180.
- Andronic, A., Braun-Munzinger, P., Gündüz, D., Kirchhoff, Y., Köhler, M. K., Stachel, J., and Winn, M. (2021). Influence of modified light-flavor hadron spectra on particle yields in the statistical hadronization model. *Nuclear Physics A* 1010, 122176.
- Andronic, A., Braun-Munzinger, P., Stachel, J., and Stocker, H. (2011). Production of light nuclei, hypernuclei and their antiparticles in relativistic nuclear collisions. *Physics Letters B* 697, 203–207.
- Anielski, J. (2015). Multiplicity Dependence of (Anti-)Deuteron Production in p+Pb Collisions at $\sqrt{s_{NN}} = 5.02$ TeV Measured with ALICE. *Journal of Physics: Conference Serie* 612(1), 012014.
- Anticic, T., Baatar, B., Bartke, J., Beck, H., Betev, L., Białkowska, H., Blume, C., Boimska, B., Book, J., Botje, M., Christakoglou, P., Chung, P., Chvala, O., Cramer, J. G., and Eckardt, V. et al. (2016). Production of deuterium, tritium, and He3 in central Pb + Pb collisions at 20A, 30A, 40A, 80A, and 158A GeV at the CERN Super Proton Synchrotron. *Physics Review C* 94(4), 044906.

- Back, B. B., Betts, R. R., Chang, J., Chang, W. C., Chi, C. Y., Chu, Y. Y., Cumming, J. B., Dunlop, J. C., Eldredge, W., Fung, S. Y., Ganz, R., Garcia, E., Gillitzer, A., Heintzelman, G., and Henning, W. F. et al. (2001). Baryon Rapidity Loss in Relativistic Au + Au Collisions. *Physical Review Letters* 86, 1970–1973.
- Barnett, R. M., Carone, C. D., Groom, D. E., Trippe, T. G., Wohl, C. G., Armstrong, B., Gee, P. S., Wagman, G. S., James, F., Mangano, M., Mönig, K., Montanet, L., Feng, J. L., Murayama, H., and Hernández, J. J. et al. (1996). Review of Particle Physics. *Physical Review D* 54, 1–708.
- Barrette, J., Bellwied, R., Braun-Munzinger, P., Cleland, W. E., Cormier, T., Dadusc, G., David, G., Dee, J., Diebold, G. E., Dietzsch, O., Duek, E., Fatyga, M., Fox, D., Greene, S. V., and Germani, J. V. et al. (1993). Antiproton production in relativistic Si-nucleus collisions. *Physical Review Letters* 70, 1763–1766.
- Bass, S., Belkacem, M., Bleicher, M., Brandstetter, M., Bravina, L., Ernst, C., Gerland, L., Hofmann, M., Hofmann, S., Konopka, J., Mao, G., Neise, L., Soff, S., Spieles, C., and H. Weber, et al. (1998). Microscopic models for ultrarelativistic heavy ion collisions. *Progress in Particle and Nuclear Physics* 41, 255-369.
- Bennett, M. J., Pope, J. K., Beavis, D., Carroll, J. B., Chiba, J., Chikanian, A., Crawford, H. J., Cronqvist, M., Dardenne, Y., Debbe, R., Doke, T., Engelage, J., Greiner, L., Hayano, R. S., and Hallman, T. J. et al. (1998). Light nuclei production in relativistic Au+nucleus collisions. *Physical Review C* 58, 1155–1164.
- Bleicher, M., Spieles, C., Jahns, A., Mattiello, R., Sorge, H., Stoecker, H., and Greiner, W. (1995). Phase space correlations of anti-deuterons in heavy ion collisions. *Physics Letters B* 361, 10–13.
- Bleicher, M. and Stoecker, H. (2002). Anisotropic flow in ultrarelativistic heavy ion collisions. *Physics Letters B* 526, 309–314.

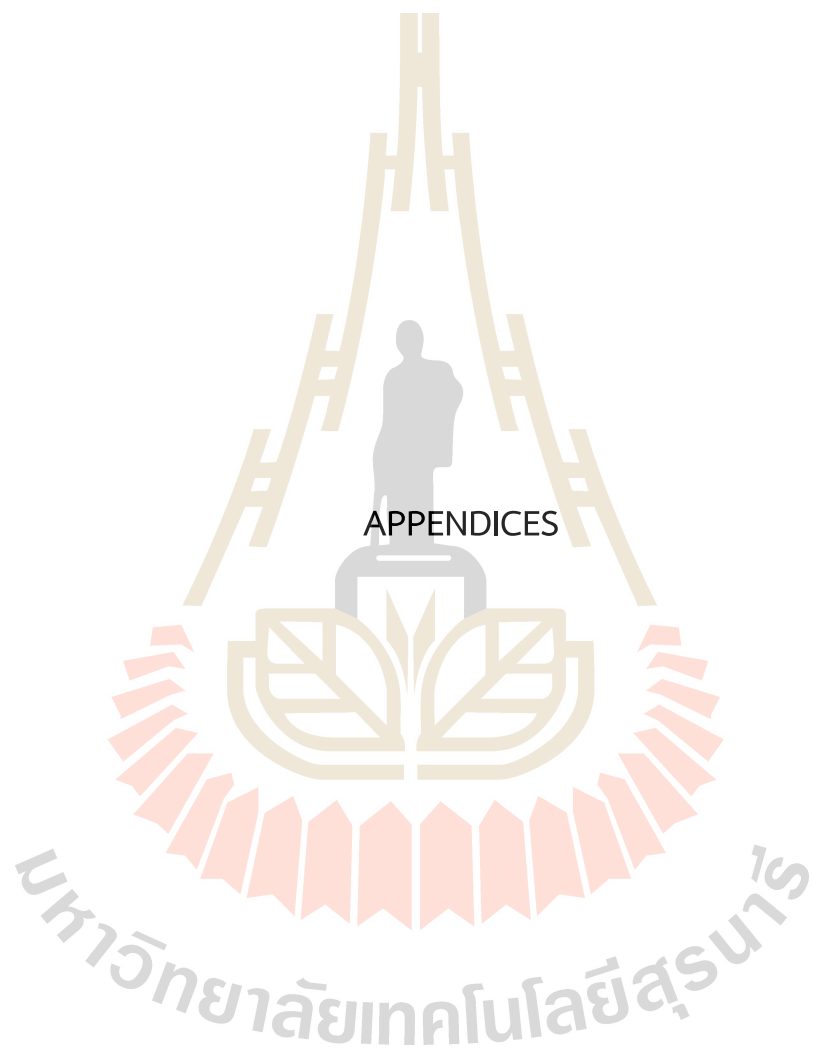
- Bleicher, M., Zabrodin, E., Spieles, C., Bass, S. A., Ernst, C., Soff, S., Bravina, L., Belkacem, M., Weber, H., Stöcker, H., and Greiner, W. (1999). Relativistic hadron-hadron collisions in the ultra-relativistic quantum molecular dynamics model. *Journal of Physics G: Nuclear and Particle Physics* 25(9), 1859–1896.
- Born, K. D., Laermann, E., Sommer, R., Zerwas, P. M., and Walsh, T. F. (1994). The Interquark potential: A QCD lattice analysis. *Physics Letters B* 329, 325–331.
- Caliandro, R., Andersen, E., Armenise, N., Ban, J., Barberis, D., Beker, H., Beusch, W., Bloodworth, I. J., Bohm, J., Campbell, M., Cantatore, E., Carrer, N., Catanesi, M. G., Chesi, E., and Dameri, M. et al. (1999). Lambda, Xi and Omega production at mid-rapidity in Pb+Pb and p+Pb collisions at 158A GeV/c. *Journal of Physics G* 25, 171–180.
- Cheng, M., Christ, N. H., Datta, S., van der Heide, J., Jung, C., Karsch, F., Kaczmarek, O., Laermann, E., Mawhinney, R. D., Miao, C., Petreczky, P., Petrov, K., Schmidt, C., and Umeda, T. (2006). Transition temperature in QCD. *Physical Review D* 74(15), 054507.
- Chomaz, P., Colonna, M., and Randrup, J. (2004). Nuclear spinodal fragmentation. *Physics Reports* 389, 263–440.
- Cleymans, J., Oeschler, H., and Redlich, K. (1999). Influence of impact parameter on thermal description of relativistic heavy ion collisions at (1-2) A-GeV. *Physical Review C* 59, 1663.
- Close, F. E. (1979). An Introduction to Quarks and Partons.
- Evans, D., Andrighetto, A., Antinori, F., Bayes, A. C., Beusch, W., Bohm, S., Caliandro, R., Carrer, N., de la Cruz, B., Davies, J. P., Bari, D. D., Elia, D., Evans, D., Fanebust, K., and R. A. Fini, et al. (1999). Enhancement of strange and multi-strange hyperons and anti-hyperons in S-S and S-W interactions at 200 GeV/c. *Journal of Physics G* 25, 209-216.

- Gabler, F., Bachler, J., Barna, D., and Barnby, L. (1999). Xi⁻ and Antixi⁺ production in Pb + Pb collisions at 158-GeV per nucleon. *Journal of physics G* 25, 199–207.
- Glen, B. (2017). How is the kurtosis of a distribution related to the geometry of the density function?
- Goulianos, K. A. (1983). Diffractive Interactions of Hadrons at High-Energies. *Physics Reports* 101, 169.
- Gross, D. J. and Wilczek, F. (1973). Ultraviolet Behavior of Nonabelian Gauge Theories. *Physical Review Letters* 33, 1343-1346.
- Gyulassy, M., Frankel, K., and Remler, E. a. (1983). DEUTERON FORMATION IN NUCLEAR COLLISIONS. *Nuclear Physics A* 42, 596–611.
- Henning, S. et al. (1978). Production of Deuterons and anti-Deuterons in Proton Proton Collisions at the CERN ISR. *Lettere al Nuovo Cimento* 21, 189.
- Hong, B., Herrmann, N., Ritman, J. L., Best, D., Gobbi, A., Hildenbrand, K. D., Kirejczyk, M., Leifels, Y., Pinkenburg, C., Reisdorf, W., Schüll, D., Sodan, U., Wang, G. S., Wienold, T., and Alard, J. P. et al. (1998). Stopping and radial flow in central Ni⁵⁸ + Ni⁵⁸ collisions between 1A and 2A GeV. *Physical Review C* 57, 244–253.
- Ko, C., Lin, Z., and Oh, Y. (2010). Transport model study of deuteron production in relativistic heavy ion collisions. *Nuclear Physics A* 834(1-4), 253c–256c.
- Koch, P. and Dover, C. B. (1989). K[±], \bar{p} and Ω^- Production in Relativistic Heavy Ion Collisions. *Physical Review C* 40, 145–155.
- Koch, V. (2010). Hadronic Fluctuations and Correlations, pages 626–652.
- Kormilitzin, A., Levin, E., and Rezaeian, A. H. (2011). On the Nuclear Modification Factor at RHIC and LHC. *Nuclear Physics A* 860, 84-101.
- Liu, H., Ajitanand, N. N., Alexander, J., Anderson, M., Best, D., Brady, F. P., Case, T., Caskey, W., Cebra, D., Chance, J., Cole, B., Crowe, K., Das, A., Draper, J., and Gilkes, M. et al. (2000). Sideward Flow in Au + Au Collisions between 2A and 8A GeV. *Physical Review Letters* 84, 5488–5492.

- Luo, X. (2012). Error Estimation for Moments Analysis in Heavy Ion Collision Experiment. *Journal of Physics G* 39, 025008.
- Luo, X. and Xu, N. (2017). Search for the QCD Critical Point with Fluctuations of Conserved Quantities in Relativistic Heavy-Ion Collisions at RHIC : An Overview. *Nuclear Science and Techniques* 28(8), 112.
- Margetis, S., Appelshauser, H., Bachler, J., Bailey, S. J., Barna, D., Barnby, L. S., Bartke, J., Barton, R. A., Bialkowska, H., Billmeier, A., Blyth, C. O., Bock, R., Bormann, C., Brady, F. P., and Brockmann, R. et al. (1999). Strangeness measurements in NA49 experiment with Pb projectiles. *Journal of Physics G Nuclear Physics* 25(2), 189-197.
- Mrowczynski, S. (1993). Anti-nucleon sources in heavy ion collisions. *Physics Letters B* 308, 216–219.
- Nagle, J. L., Kumar, B. S., Bennett, M. J., Coe, S. D., Diebold, G. E., Pope, J. K., Jahns, A., and Sorge, H. (1994). Anti-deuteron production in high-energy heavy ion collisions. *Physical Review Letters* 73, 2417-2420.
- Nayak, T. K. (2020). Probing the QCD phase structure using event-by-event fluctuations. *Journal of Physics: Conference Series* 1602(1), 012003.
- Perkins, D. H. (1982). Introduction to high energy physics.
- Poskanzer, A. M. and Voloshin, S. A. (1998). Methods for analyzing anisotropic flow in relativistic nuclear collisions. *Physical Review C* 58, 1671–1678.
- Randrup, J. (2004). Spinodal decomposition during the hadronization stage at RHIC? *Physical Review Letters* 92, 122301.
- Retinskaya, E., Luzum, M., and Ollitrault, J.-Y. (2012). Directed flow at midrapidity in $\sqrt{s_{NN}} = 2.76$ TeV Pb+Pb collisions. *Physical Review Letters* 108, 252302.
- Sasaki, C., Friman, B., and Redlich, K. (2007). Density fluctuations in the presence of spinodal instabilities. *Physical Review Letters* 99, 232301.

- Sato, H. and Yazaki, K. (1981). On the coalescence model for high-energy nuclear reactions. *Physics Letters B* 98, 153–157.
- Schwinger, J. (1951). On gauge invariance and vacuum polarization. *Physical Review* 82(5), 664.
- Sheskin, D. J. (2003). Handbook of parametric and nonparametric statistical procedures. Chapman and Hall/CRC.
- Shiva, K. B., Beavis, D., Bennett, M., Carroll, J., Chiba, J., Crawford, H., Debbe, R., Doke, T., Engelage, J., and Greiner, L. (1994). Rapidity distributions of antiprotons in Si+ A and Au+ A collisions. *Nuclear Physics A* 566, 439c–442c.
- Shuryak, E. and Torres-Rincon, J. M. (2020). Light-nuclei production and search for the QCD critical point. *The European Physical Journal A* 56(9), 241.
- Shuryak, E. V. (1978). Quark-Gluon Plasma and Hadronic Production of Leptons, Photons and Psions. *Physical Review Letters* B 78, 150.
- Steinheimer, J., Gudima, K., Botvina, A., Mishustin, I., Bleicher, M., and Stocker, H. (2012). Hypernuclei, dibaryon and antinuclei production in high energy heavy ion collisions: Thermal production versus Coalescence. *Physics Letters B* 714, 85–91.
- Steinheimer, J. and Randrup, J. (2012). Spinodal amplification of density fluctuations in fluid-dynamical simulations of relativistic nuclear collisions. *Physical Review Letters* 109, 212301.
- Stephanov, M. A. (2004). QCD phase diagram and the critical point. *Progress of Theoretical Physics Supplement* 153, 139–156.
- Stephanov, M. A. (2009). Non-Gaussian fluctuations near the QCD critical point. *Physical Review Letters* 102, 032301.
- Stephanov, M. A. (2011). On the sign of kurtosis near the QCD critical point. *Physical Review Letters* 107, 052301.

- Stephanov, M. A., Rajagopal, K., and Shuryak, E. V. (1998). Signatures of the tricritical point in QCD. *Physical Review Letters* 81, 4816-4819.
- Wang, D.-F., Zhang, S., and Ma, Y.-G. (2020). Nuclear system size scan for freeze-out properties in relativistic heavy-ion collisions by using a multiphase transport model. *Physical Review C* 101(3), 034906.
- Yin, X., Ko, C. M., Sun, Y., and Zhu, L. (2017). Elliptic flow of light nuclei. *Physical Review C* 95(5), 054913.
- Yu, N. (2017). Beam energy dependence of d and \bar{d} productions in Au+Au collisions at RHIC. *Nuclear Physics A* 976, 788–791.
- Zabrodin, E. E., Bravina, L. V., Kodolova, O. L., Kruglov, N. A., Proskuryakov, A. S., Sarycheva, L. I., Bogolubsky, M. Y., Levitsky, M. S., Maksimov, V. V., Minaenko, A. A., Moiseev, A. M., and Chekulaev, S. V. (1995). Inclusive spectra of charged particles in pp and $p\bar{p}$ interactions at 32 GeV/c. *Physical Review D* 52, 1316–1342.
- Zhu, L., Ko, C. M., and Yin, X. (2015). Light (anti-)nuclei production and flow in relativistic heavy-ion collisions. *Physical Review C* 92(6), 064911.
- Zyla, P., Barnett, R., Beringer, J., Dahl, O., Dwyer, D., Groom, D., Lin, C., Lugoosky, K., Pianori, E., Robinson, D., Wohl, C., Yao, W., Agashe, K., Aielli, G., and Allanach, B. et al. (2020). Review of Particle Physics. *Progress of Theoretical and Experimental Physics* 2020(8), 083C01.



APPENDIX A

LORENTZ TRANSFORMATION

In this thesis, the Lorentz transformation is used to convert between the center of mass frame (CM) and laboratory frame (Lab). It is used to convert the rapidity and momentum distribution of the observed particle. In relativity physics, Lorentz transformations are a set of equations used to link the space and time coordinates of two systems with the same velocity.

Lorentz boost is considered in z-axis when a particle in a coordinate frame L at (t, x, y, z) is boosted to (t', x', y', z') for L' with velocity (v) . Lorentz transformation in the z-axis is defined in the form as:

$$\begin{aligned} t' &= \gamma (ct - \beta z) , \\ x' &= x, \\ y' &= y, \\ z' &= \gamma (z - \beta ct) . \end{aligned} \tag{A.1}$$

where Lorentz factor is $\gamma = \frac{1}{\sqrt{1-\beta^2}}$ and $\beta = \frac{v}{c}$. By the same way, the Lorentz transformation for a Four-Vector (E, \vec{p}) can be defined as:

$$\begin{aligned} E' &= \gamma (E - \beta p_z) , \\ p_x' &= p_x, \\ p_y' &= p_y, \\ p_z' &= \gamma (p_z - \beta E) . \end{aligned} \tag{A.2}$$

where the velocity of particle is $\beta \vec{v} = \frac{\vec{p}}{E}$ and $E^2 - |\vec{p}|^2 = m^2$.

APPENDIX B

KINEMATIC VARIABLES

In particle collisions, several kinematic variables are used in this thesis to study the properties and dynamics of particles. We consider a particle traveling in the z axis as the beam direction. The momentum in the z-direction is called the longitudinal momentum (p_z). The transverse momentum (p_t) magnitude is defined as:

$$p_t = \sqrt{p_x^2 + p_y^2}. \quad (\text{B.1})$$

As well as the transverse mass (m_t) can be defined in the form

$$m_t = \sqrt{p_t^2 + m^2}. \quad (\text{B.2})$$

We also define a quantity called the rapidity y , the rapidity of a particle is defined as:

$$y = \frac{1}{2} \ln \frac{E + p_z}{E - p_z} \quad (\text{B.3})$$

In the laboratory system the center of mass of the rapidity can be defined in the term velocity when the total energy in the center of mass is $E_{cm} = \sqrt{s}$. The energy and longitudinal momentum are $\gamma_{cm} \sqrt{s}$ and $\beta_{cm} \gamma_{cm} \sqrt{s}$ respectively. Then we get

$$y = \frac{1}{2} \ln \left[\frac{\gamma_{cm} \sqrt{s} + \beta_{cm} \gamma_{cm} \sqrt{s}}{\gamma_{cm} \sqrt{s} - \beta_{cm} \gamma_{cm} \sqrt{s}} \right] \quad (\text{B.4})$$

$$y = \frac{1}{2} \ln \left[\frac{1 + \beta_{cm}}{1 - \beta_{cm}} \right]$$

Assume a particle is emitted at an angle θ with respect to the beam's axis. Then from Equation (B.3) the rapidity can be defined as:

$$y = \frac{1}{2} \ln \left(\frac{(m^2 + p^2)^{\frac{1}{2}} + p_z}{(m^2 + p^2)^{\frac{1}{2}} - p_z} \right) \quad (\text{B.5})$$

At a highly relativistic particle, $p \gg m$ hence we get

$$\begin{aligned}
y &= \frac{1}{2} \ln \left(\frac{p(1 + \frac{m^2}{p^2})^{\frac{1}{2}} + p_z}{p(1 + \frac{m^2}{p^2})^{\frac{1}{2}} - p_z} \right), \\
&\simeq \frac{1}{2} \ln \left(\frac{1 + p_z + \frac{m^2}{2p} + \dots}{p - p_z + \frac{m^2}{2p} + \dots} \right), \\
&\simeq \frac{1}{2} \ln \left(\frac{1 + \frac{p_z}{p} + \frac{m^2}{2p^2} + \dots}{1 - \frac{p_z}{p} + \frac{m^2}{2p^2} + \dots} \right).
\end{aligned} \tag{B.6}$$

Now $p_z/p = \cos\theta$ we have

$$1 + \frac{p_z}{p} = 1 + \cos\theta = 1 + \left(\cos^2 \frac{\theta}{2} - \sin^2 \frac{\theta}{2} \right) = 2\cos^2 \frac{\theta}{2} \tag{B.7}$$

and

$$1 - \frac{p_z}{p} = 1 - \cos\theta = 1 - \left(\cos^2 \frac{\theta}{2} - \sin^2 \frac{\theta}{2} \right) = 2\sin^2 \frac{\theta}{2} \tag{B.8}$$

Substituting Equation (B.7) and (B.8) into Equation (B.6) we obtain

$$\begin{aligned}
y &\simeq \frac{1}{2} \ln \frac{\cos^2 \frac{\theta}{2}}{\sin^2 \frac{\theta}{2}} \\
&\simeq -\ln \tan \frac{\theta}{2}.
\end{aligned} \tag{B.9}$$

So that for highly relativistic particles, $y \simeq \eta$, the the pseudorapidity η can be defined as:

$$\eta = -\ln \tan \frac{\theta}{2} \tag{B.10}$$

CURRICULUM VITAE

NAME: Sukanya Sombun **GENDER:** Female

NATIONALITY: Thai **DATE OF BIRTH:** January 06, 1990

EDUCATIONS:

- B.Sc. Department of Physics, Naresuan University, 2013.
- M.Sc. Department of Physics, Naresuan University, 2016.

PUBLICATIONS

- [1] P. Srisawad, A. Harfield, S. Sombun, T. Katukum, O. Ketsungnoen, Y. M. Zheng, A. Limphirat and Y. Yan, “**Influence of the in-medium kaon potential on kaon production in heavy ion collisions**”, J. Phys. Conf. Ser. **509** (2014), 012034
- [2] S. Sombun, J. Steinheimer, C. Herold, A. Limphirat, Y. Yan and M. Bleicher, “**Higher order net-proton number cumulants dependence on the centrality definition and other spurious effects**”, J. Phys. G **45** (2018) no.2, 025101
- [3] S. Sombun, K. Tomuang, A. Limphirat, P. Hillmann, C. Herold, J. Steinheimer, Y. Yan and M. Bleicher, “**Deuteron production from phase-space coalescence in the UrQMD approach**”, Phys. Rev. C **99** (2019) no.1, 014901
- [4] S. Sombun, J. Steinheimer, C. Herold, A. Limphirat, Y. Yan and M. Bleicher, “**Influence of centrality definition and detector efficiency on the net-proton kurtosis**”, Springer Proc. Phys. **250** (2020), 335-343